REPORT
doi:10.26443/seismica.v2i4.1584

Comparisons of tsunami inundation for homogeneous and heterogeneous earthquake sources at selected sites for the Cascadia Subduction Zone

Sean R. Santellanes [*1], **Diego Melgar** [1,2], **Bruno Adriano** [3], **Brendan W. Crowell** [4], **Ronald Eguchi** [5], **Shunichi Koshimura** [3]

[1]Department of Earth Sciences, University of Oregon, Eugene, Oregon, USA, [2]Cascadia Region Earthquake Science Center, Eugene, Oregon, USA, [3]International Research Institute of Disaster Science, Tohoku University, Sendai, Miyagi, Japan, [4]School of Earth Sciences, The Ohio State University, Columbus, Ohio, USA, [5]ImageCAT Inc., Long Beach, California, USA

Author contributions: *Conceptualization*: SS, DM, BA. *Methodology*: SS,DM,BA. *Formal Analysis*: SS. *Investigation*: SS. *Writing - Original draft*: SS. *Writing - Review & Editing*: SS, DM. *Visualization*: SS. *Supervision*: DM. *Funding acquisition*: DM,BWC, RE, SK.

Abstract Tsunami hazard severity — especially tsunami inundation depth — is related to the tsunami's source mechanism. Traditionally, homogeneous earthquake rupture sources have been used as the source mechanism for tsunamis generated in the Cascadia Subduction Zone for regional hazard assessment. We show with 200 heterogeneous earthquake rupture sources how tsunami inundation hazards change for three sites located along the Cascadia Subduction Zone when the assumption of homogeneous slip is relaxed. Our results indicate that the tsunami inundation limit extends further inland compared to homogeneous sources. We also note that the 1-in-2475-year exceedance threshold extends further inland for heterogeneous earthquake rupture sources compared to official tsunami evacuation lines and the American Society of Civil Engineers tsunami design zone.

Production Editor:
Christie Rowe, Alice Gabriel
Handling Editor:
Jonathan Weiss
Copy & Layout Editor:
Théa Ragon

Signed reviewer(s):
Steven J. Gibbons

Received:
February 5, 2025
Accepted:
August 16, 2026
Published:
October 20, 2026

1 Motivation

Tsunamis of seismic origin have been among the deadliest natural hazards of 21st century. The 2004 Sumatra and 2011 Tohoku-Oki tsunamis caused over 230,000 and 22,000 casualties respectively (Mori et al., 2022). The proximity of these events to the near-shore environment meant that areas near the tsunami source had only minutes to tens of minutes to prepare before the onset of inundation. That fact, coupled with underestimation of the tsunamigenic potential of the earthquake sources, were among some of the main reasons for the high number of casualties (Yun and Hamada, 2015; Mori et al., 2022). In many ways, these past events mirror what a future Cascadia Subduction Zone (CSZ) earthquake could be like for the United States Pacific Northwest (USPNW).

Since the discovery of the CSZ tsunami hazards by those not of the American Indian or First Nations groups, USPNW state governments have mandated that hazard assessments be carried out to ensure the reduction of harm to civilians and economic centers (Priest, 1995). It was these mandates that led to the creation of the first tsunami evacuation maps in 1995 by the Oregon Department of Geologic and Mineral Industries (DOGAMI) at the behest of the Oregon legislature. These first assessments reflected the science of their time, as knowledge about the CSZ fault structure was still in its infancy, bathymetry and topography data were still of limited resolution, and the paleoseismic record not yet fully established to discern its seismogenic behavior. As the science has matured, the USPNW state legislatures have adopted building codes with focuses on flow depth (henceforth, "inundation depth," which is the water column above the mean high water line) (Figure 1), flow velocity, and extraordinary debris impacts (Priest and Allan, 2019; American Society of Civil Engineers, 2022). Because details of the slip patterns of future CSZ events are not known, and difficult if not impossible to predict, these assessments use the simplifying assumption of homogeneous or quasi-homogeneous slip distributions. Here quasi-homogeneous refers to those slip distributions that appear homogeneous but have tapers applied to various parts. For example, the XL1 "t-shirt" model, as shown in Witter et al. (2011) and Witter et al. (2013), is a well-known quasi-homogeneous slip distribution. Importantly, over the last decade, this assumption has been shown to be too gross of an oversimplification of large earthquake ($\geq$M7.0) rupture processes (Mai and Thingbaijam, 2014; Ye et al., 2016; Hayes, 2017). Part of the reason that this assumption was made in past hazards assessments was due to the lack of adequate

*Corresponding author: ssantel2@uoregon.edu

computational resources; however, this specific issue has abated with the advent of computationally efficient CPU/GPUs, tsunami modeling, and earthquake rupture algorithms. Furthermore, it has been shown that both in the near- and far-field of large earthquakes homogeneous slip systematically increases the tsunami amplitude (Melgar et al., 2019; Davies and Griffin, 2020). In this paper, we will detail the history of homogeneous rupture types used for hazards assessments in the USPNW and advocate, through new modeling, for why the scientific and engineering communities must consider down-weighting them in favor of fully heterogeneous slip models in future and forthcoming scenario events as well as in probabilistic tsunami hazard analysis (PTHA).

1.1 History of homogeneous ruptures in the Pacific Northwest

Extensive effort has been made to reconstruct the paleoseismic history of the CSZ, leading it to have some of the most complete paleoseismic records for a subduction zone in the world (Kelsey et al., 2005; Atwater and Griggs, 2012; Goldfinger et al., 2012; Witter et al., 2013; Walton et al., 2021). From these records, we know of 19-20 full-margin rupture scenarios that have occurred over the previous 10,000 years (Goldfinger et al., 2012; Walton et al., 2021). This information has been used as justification for full-margin rupture models to produce a series of 15 rupture scenarios representative of the previous 10,000 years of tsunami hazards (Witter et al., 2011, 2013). These models produced by DOGAMI are often referred to as the "t-shirt" models because they detail a series of ruptures ranging from small ("SM") to extra-extra-large ("XXL") with three types of ruptures: splay fault ("1"), shallow buried rupture ("2"), and deep buried rupture ("3") (Witter et al., 2011, 2013), thus event "L2", for example, is a shallow buried "large" scenario. These models served as the backbone for the hazard assessments performed by the states of Washington and Oregon prior to the adoption of the American Society of Civil Engineers (ASCE) tsunami design load guidelines 7-16/7-22 in 2021/2022.

Starting in 1995, DOGAMI was bound by Oregon law to use the "Maximum Considered Tsunami" (MCT) (House Bill 379), until 2019 when this law was repealed (House Bill 3309). This former law had focused efforts of DOGAMI and university partners on performing research to discern what the MCT of the CSZ is. The research carried out by Priest (1995) was later superseded by the work of Witter et al. (2011) and Witter et al. (2013) when it became clear that the CSZ can potentially produce XXL rupture scenarios of moment magnitude M_w9.2. From that research, the state of Oregon selected the XXL1 scenario as the basis for its tsunami evacuation lines, as it was legally bound to choose the MCT inundation elevation for its risk tolerance. Currently, Oregon has adopted a 1-in-2475-year event based on the ASCE 7-22 framework (House Bill 2605).

The state of Washington Department of Natural Resources (WaDNR) is likewise bound by its state government's law, which also refers to an MCT. WaDNR must consider an MCT within a 2,475-year mean return period (MRP), or a probabilistic tsunami not to exceed 2% over a 50-year period, or a deterministic MCT that can reasonably affect a site. To meet legal requirements, WaDNR worked together with DOGAMI and university partners to select the L1 model as representative of its tsunami risk tolerance for the southern Washington coast. Although the L models have an MRP of 3,333-year, WaDNR is legally required to treat it as a 2,475-year MRP event (Eungard et al., 2018). However, both the states of Oregon and Washington are in the process of performing a more complex PTHA to establish an MCT that follows the U.S. Geological Survey (USGS) Powell Center's CSZ logic tree (Sypus and Wang, 2024).

The state of California, unlike its USPNW neighbors, does not give its state agencies a legal framework for tsunami risk. Instead, they delegate this authority to the counties, and they can choose MRPs of 975-year or 2475-year (Thio and Somerville, 2009). Coastal communities can then select their desired risk level. They select a "worst-case" scenario, add an additional safety factor, and receive community input to produce their evacuation lines. The second-generation tsunami evacuation maps for that state were produced at a time when paleoseismic and geodetic records had yet to be combined. And so, their maps are agnostic to the even more extreme MCT scenarios as seen in Witter et al. (2011) and Witter et al. (2013). Thio and Somerville (2009) noted the limitations of their work and stated that the issue be revisited when more knowledge was available. Much like Oregon and Washington, they are in the process of performing a PTHA study that will serve as a new basis for 975-year and 2475-year events.

Beyond the above issues, which relate to how tsunami evacuation zones are demarcated, in recent years, the five Pacific bordering states have started the process of adopting the ASCE building codes which contain new provisions regarding tsunamis (ASCE 7-22). These provisions provide rules for the establishment of tsunami design zones (TDZs). TDZ limits are determined by where the inundation depth goes to 0 m, so the TDZ limits are essentially the same as the horizontal extent of the inundation limit (Figure 1). However, USPNW states differ on whether to use the TDZ developed by the ASCE or their local states (e.g., as is the case with WaDNR). Within TDZs, buildings must be built to withstand tsunami loads if they fall into Risk Category II, III, or IV. For context, Risk Category I buildings generally include temporary buildings, agricultural facilities, and minor storage facilities. Risk Category II buildings are buildings with fewer occupants and smaller buildings whose functions are nonessential for responding to emergencies (e.g., fast-food restaurants). Risk Category III buildings are nonessential buildings that have high occupancy and large building sizes (e.g., schools). Risk Category IV buildings are essential buildings, such as hospitals, fire and rescue, and police stations that must be operable in the event of an emergency. Risk Category II buildings must be built to ASCE 7-22 if they have a mean height of 19.8 m above mean high water and inundation depth > 1 m. Risk Category III if inundation depth > 1 m. Risk Category IV buildings must always

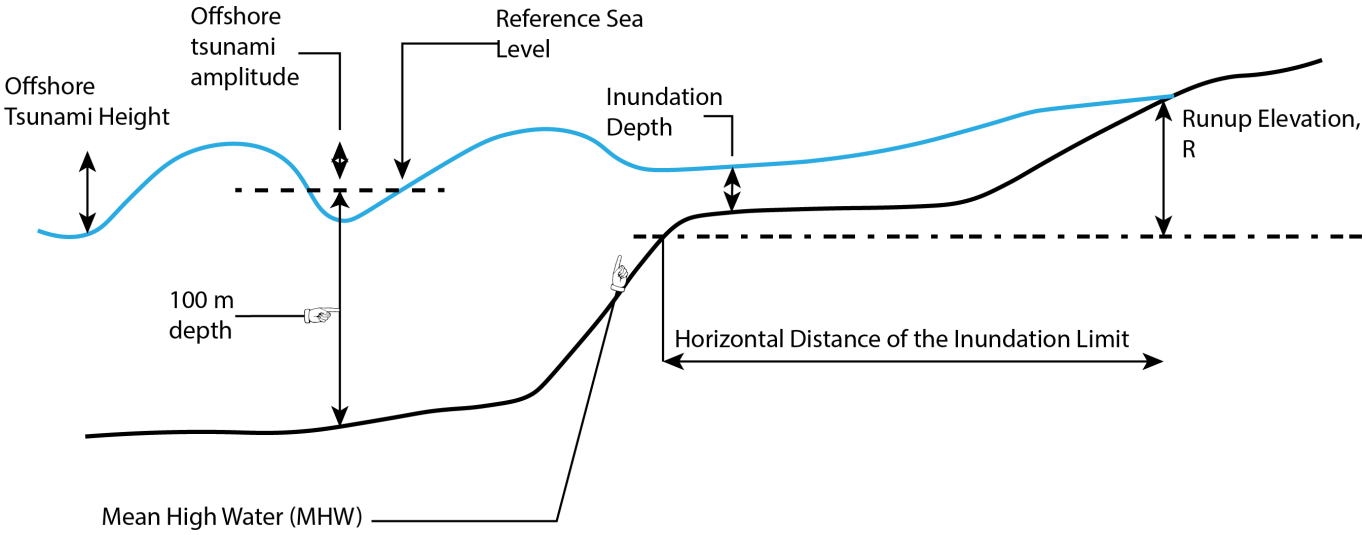

Figure 1 Schematic diagram adapted from American Society of Civil Engineers (2022). We adopt their use of terms in order to be consistent with their terminology (page 25, American Society of Civil Engineers, 2022).

be built to code (American Society of Civil Engineers, 2022).

ASCE 7-22 utilizes 372 rupture scenarios and performs hydrodynamic modeling to the offshore 100 m depth contour tsunami amplitudes with projections using Green's law onto the near-shore environment for inundation extent (American Society of Civil Engineers, 2022). The ASCE tsunami scenarios utilize the 1 cm/yr and top of non-volcanic tremor geodetic locking models to determine the extent of slip in a CSZ earthquake (Priest and Allan, 2019; American Society of Civil Engineers, 2022).

ASCE 7-22 has noted that the DOGAMI models lack some realism by not including varying bottom friction in calculating tsunami inundation, claiming that this leads to models that over-extend the spatial extent of inundation. Instead, ASCE 7-22 relies on statistical calibration of tsunami inundation that includes land use/cover effects, which they state is a more realistic representation of tsunami inundation behavior (American Society of Civil Engineers, 2022). This notwithstanding, the DOGAMI models have recently been shown to produce realistic inundation models when compared to the distribution of sandy deposits at paleoseismic sites such as the Salmon River estuary by La Selle et al. (2024). So, contemporary tsunami modeling setups should be able to produce realistic tsunami inundation extents to a better degree than was what available in 2012/2013 (Witter et al., 2013; La Selle et al., 2024).

Both DOGAMI and ASCE use homogeneous or quasi-homogeneous slip distributions as their earthquake sources – these are widely used by the scientific and engineering communities to establish best practices when it comes to land use, building codes, and validation of paleoseismic data. However, as we will show in the next sections, both types of models rely on assumptions that can potentially underestimate tsunami inundation limits. It is this systemic over-simplification of earthquake source complexity that can lead to inaccuracies in probabilistic assessments of tsunami hazards. We will find that, to construct robust assessments, heterogeneous source complexity must be fully considered.

1.2 Source complexity and geodetic coupling in local tsunami hazard estimates

ASCE 7-22 utilizes simplistic sources. It is not uncommon to use homogeneous ruptures in tsunami hazards assessments for the CSZ. The 1995 work of DOGAMI utilized a similar simplistic, homogeneous rupture for its first iteration of tsunami evacuation lines (Priest, 1995). As new tectonic and geodynamic details were revealed about the CSZ, the second-generation models adopted a quasi-homogeneous source with slip varying smoothly along dip and considering splay faults and other complexities (Witter et al., 2011, 2013). These models reflected the science of their time and were well justified. We now know that source complexity increases for $> M_w 7$ (Mai and Thingbaijam, 2014; Ye et al., 2016; Hayes, 2017).

Local tsunami hazard estimates performed by the USPNW states have yet to formally include more advanced source complexity (Thio and Somerville, 2009; Witter et al., 2011; Eungard et al., 2018). The impacts of this have been addressed by the tsunami community fairly extensively (Li et al., 2016; LeVeque et al., 2017; Sepúlveda et al., 2017; Melgar et al., 2019; Becerra et al., 2020; Davies and Griffin, 2020; Small and Melgar, 2021; Goda, 2022; Small and Melgar, 2023). Here, by "complexity" we mean better approximations of fault slip distribution heterogeneity. Large earthquakes can have patches of high co-seismic slip which can in turn cause areas of higher tsunami excitation (LeVeque et al., 2017; Small and Melgar, 2021); likewise, areas near patches of low coseismic slip may have lower tsunami inundation runup. Additionally, previous work has shown that earthquake source complexity can be potentially anticipated by considering the present-day state of coupling of the subduction zone fault interface as shown for Japan (Loveless and Meade, 2015), Alaska (Li and Frey-

mueller, 2018), Chile (Métois et al., 2013; Barnhart et al., 2016), and Peru (Perfettini et al., 2010; Villegas-Lanza et al., 2016). Although, some of these subduction are not well constrained due to the lack of data. Generally, areas with high coupling are perceived as more "hazardous" and expected to produce larger slip in future events.

Several competing hypotheses exist related to interseismic coupling (i.e., how stuck the two tectonic plates are between each other) behavior of the CSZ. Since the beginning of the 21^{st} century, global navigation satellite system (GNSS) stations have been deployed en masse throughout the USPNW. The associated geodetic data facilitate the creation of kinematic fault coupling models(Schmalzle et al., 2014; Frankel et al., 2015; Li et al., 2018; Lindsey et al., 2021). Without adequate GNSS coverage of the offshore environment, these models have taken differing approaches to account for trench locking behaviors. These have been shown to lead to differing values for not only tsunami inundation but also coastal surface displacement (Small and Melgar, 2021). Despite this, we can use the GNSS-based fault coupling models to explore a larger variation of potential tsunami inundation scenarios (or particles) by generating stochastic models that use fault coupling as "preconditions" to produce spatially variable fault slip models (Small and Melgar, 2021; Melgar, 2021). From here on out, the term particles is used to refer to the heterogeneous sources. This is because in literature, the preferred term is particle for ensembles, and we enforce it here so that the reader adopts a more statistic-minded approach (Van Leeuwen, 2009). In addition, it reduces confusion between the deterministic "t-shirt" models and the particle statistics we show later on.

1.3 Are the ASCE 7-22 and DOGAMI "t-shirt" models still reasonable sources for hazards estimates?

Given what we have discussed about the state of homogeneous and heterogeneous slip models, the central question addressed in this work is are the models reasonably approximated? The USPNW states are making preparations to use the ASCE 7-22 models as their de jure (i.e., lawful) building codes. Meanwhile, the "t-shirt" models continue to serve as the backbone of tsunami evacuation risk tolerances for Washington and Oregon. Efforts are currently underway to make future ASCE 7 building codes better informed with DOGAMI models (Petersen et al., 2024). Although, we cannot explore the ASCE 7-22 models, we can infer what they look like from conference proceedings and documents. Of which, we know that the 372 models they used for ASCE 7-22 are homogeneous models based on the 2014 and 2018 USGS National Seismic Hazard Maps, and that they select a 1-in-2475-year exceedance (note the shift from MRP — previous legislation in the USPNW uses both interchangeably) due to seismic hazard analysis using the same number (Priest and Allan, 2019; American Society of Civil Engineers, 2022). The logic tree for ASCE 7-16/22 (Figure 2-8 in Priest and Allan, 2019) details the use of two variations of the 1 cm/yr model: the mid-point of the fully locked zone and the 1 cm/yr contour. The third

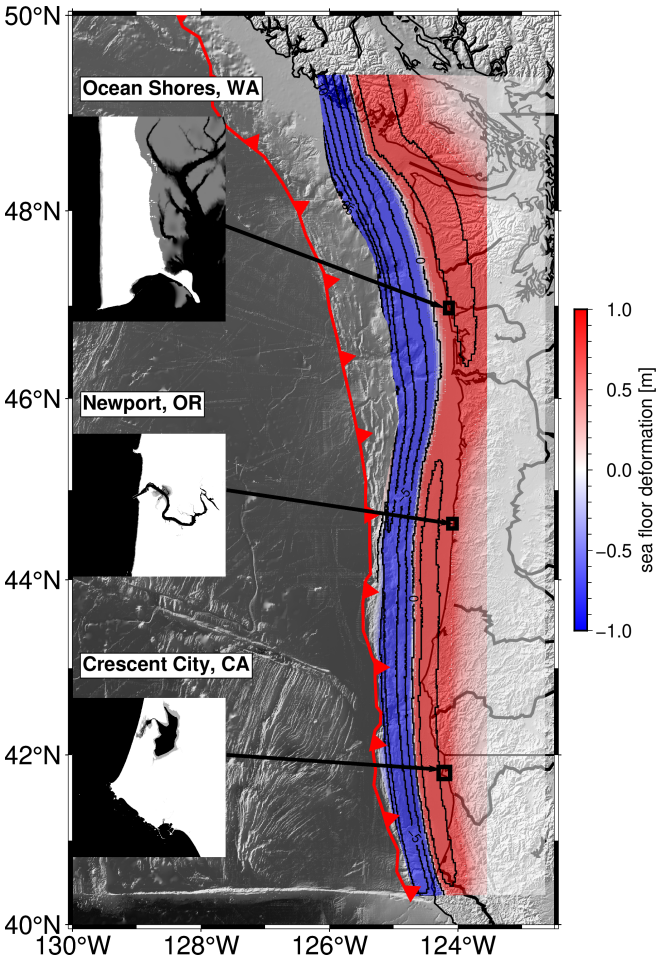

Figure 2 Map of the study area. Insets show the areas of interest that were used for modeling of tsunami inundation. Black arrows point from the inset to the locations of the areas of interest on the main map. The Cascadia Subduction Zone (CSZ) is denoted by the red subduction zone symbols. The L1 "t-shirt" vertical deformation model is shown by the polar plot. As per Witter et al. (2011), the L1 model is a rupture scenario that is between M_w9.0-9.1, and it has co-seismic slip terminating at a proposed mega-splay fault. Contours are plotted every 2.5 m, with annotations every 5 m. The L1 model is clipped such that there is no deformation past the proposed splay fault from Witter et al. (2011). This map was constructed using GMT 6 (Wessel et al., 2019).

they use is the top of non-volcanic tremor zone. However the rupture models are not publicly available, so we only analyze the DOGAMI "t-shirt" models.

When we compare the XXL1 "t-shirt" from Figure 2 with the heterogeneous sources seen in Figure 3, we see the spatial variations between slip and vertical displacement between the two, and how these poise significant differences between tsunami inundation behaviors. The "t-shirt" models have three major caveats: (1) they model slip quasi-homogeneously, (2) they were not informed by (then unknown) geodetic constraints, and (3) they do not consider more frequent ruptures on either the northern (Atwater and Griggs, 2012) or southern sections (Goldfinger et al., 2012) of the CSZ. We also know that ASCE 7-22 must suffer from similar problems, as they claim to use the 2014 and 2018 USGS National Seismic Hazard Maps for their events, which do not use

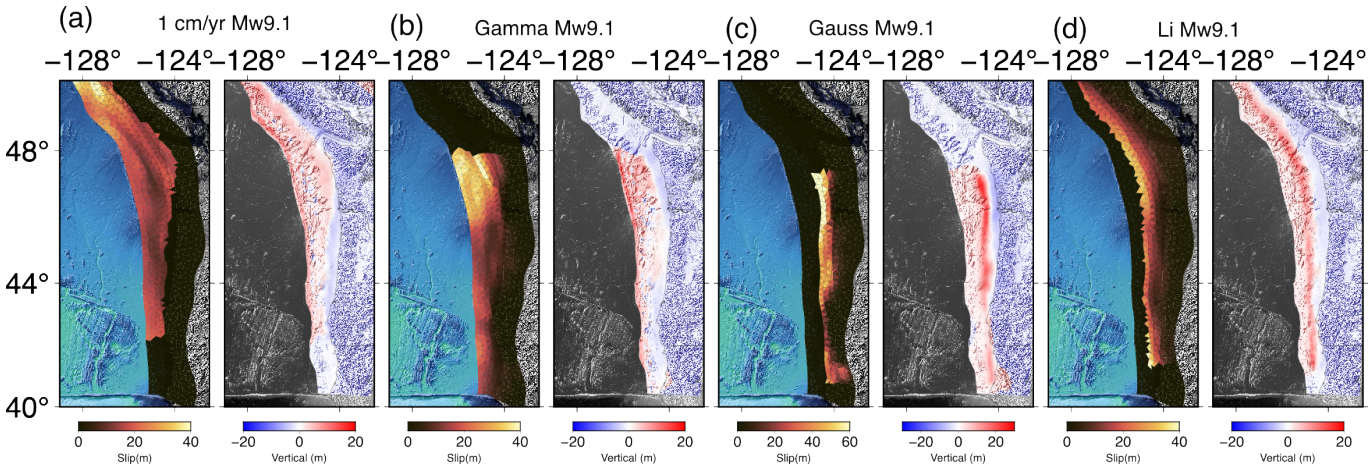

Figure 3 Heterogeneous slip and vertical deformation maps for the four geodetic families used in this study. M_w9.1 source ruptures for (a) 1 cm/yr (Frankel et al., 2015), (b) Gamma (Schmalzle et al., 2014), (c) Gauss (Schmalzle et al., 2014), and (d) Li (Li et al., 2018) geodetic models. Subduction zone interface geometry comes from Hayes et al. (2018). These maps were constructed using GMT 6 (Wessel et al., 2019).

any advances proposed by Goldfinger et al. (2017) and Nelson et al. (2021).

In this study, we will show that heterogeneous slip from 200 stochastic particles leads to varying horizontal inundation limits at three sites — Ocean Shores, WA; Newport, OR; and Crescent City, CA — compared to the DOGAMI rupture models (Figure 2). We show that the XL1 scenario has inundation depths $> 90^{\text{th}}$ percentile compared to an ensemble of M_w comparable heterogeneous sources. Meanwhile, the L1 scenario has inundation depths that are in the 45^{th}-75^{th} percentile compared; likewise compared to an ensemble of M_w comparable heterogeneous sources. We then compute probabilistic tsunami hazard curves and exceedance maps for the three sites. Our maps differ slightly from the official tsunami evacuation lines for Newport, OR and Ocean Shores, WA. However, we find that Crescent City, CA's tsunami evacuation lines do not adequately capture the exceedance faced by heterogeneous rupture of the CSZ.

2 Data and Methods

2.1 Stochastic modeling of geodetically constrained ruptures

We use the FakeQuake methodology described by Melgar et al. (2016b) and Goldberg and Melgar (2020) and applied by Small and Melgar (2021) and validated by Small and Melgar (2023) for modeling stochastic sources used in this study. We consider ruptures generated by four geodetic coupling models: "1 cm/yr" (Frankel et al., 2015), "Gauss" (Schmalzle et al., 2014), "Gamma" (Schmalzle et al., 2014), and "Li" (Li et al., 2018). The "1 cm/yr" model details the 1cm/yr coupling contour (25% coupling) limit of slip, as shown by Frankel et al. (2015). This model follows the assumption that no coseismic slip extends deeper than the 1 cm/yr contour (Frankel et al., 2015). As a result, the model has no along-strike variability, meaning that slip is likely everywhere where mean slip is not 0 (Frankel et al., 2015; Melgar et al., 2016a). The "Gauss" model enforces a Gaussian distribution of locking with depth, and it penalizes slip to enforce mean locking above the 30 km depth contour (Schmalzle et al., 2014). The "Gamma" model enforces that the megathrust is fully locked with large slip deficits at the CSZ trench that they decay monotonically with an assumed gamma shape factor(Schmalzle et al., 2014). The "Li" model uses a viscoelastic approach to model trench locking(Li et al., 2018). These three models have varying along-strike maximum slip depths, and they vary the strength of locking along-dip and along-strike (Schmalzle et al., 2014; Li et al., 2018)(Figure 3). Small and Melgar (2021) note that models constrained by geodetic locking do not have coseismic slip that follows the pattern of interseismic locking one to one. Instead, they detail that higher locking areas have more frequent high slip. By using these geodetic constraints, we make the assumption that the slip in the next CSZ earthquake will be at least somewhat correlated with one of these models. Unfortunately, the validity of the geodetic coupling models is unknown due to absence seafloor geodetic measurements.

For each of the four mean models of choice, we generate 25 ruptures with moment magnitudes that fall into either the L ($M_w 9.0-9.1$) or XL ($M_w 9.1-9.2$) classifications described by Witter et al. (2011) and Witter et al. (2013) for a total of 200 inundation scenarios (or particles). We highlight that 200 particles are not sufficient to detail the entire realm of seismogenic behavior of the CSZ. However, the goal of this study is to detail inundation related impacts. Davies (2019) contains a more detailed analysis of how many scenarios and modeling schemes may be necessary to do so. We select the XL scenario over the XXL scenario because the XXL scenarios are not constrained by the paleoseismic and turbidite records (Witter et al., 2013). Rather, they make the assumption that no slip has been accommodated by southern ruptures of the CSZ (Witter et al., 2013). To accommodate this slip, the XL scenario tapers off coseismic slip for the southern section of the CSZ (Witter et al., 2013), so we select it to compare against the heterogeneous sources. As the only difference between

the XL and XXL classes is this tapering, the heterogeneous XL-like sources can take on behavior akin to an XXL class event, which we allow for a full exploration of tsunami inundation range. We set the M_w bins for the L-like particles as $9.0 \leq M_w < 9.1$, and for the XL-like particles $9.1 \leq M_w \leq 9.2$. We disregard length and width estimates of the L and XL classes to allow for large slip, compact area events in the northern and southern sections of the CSZ. We follow the logic of Witter et al. (2013) and Eungard et al. (2018) and set the annualized rate of occurrence for L-like particles to 1-in-3,333 years and for XL-like particles to 1-in-5,000 years. We choose the Slab 2.0 geometry of Hayes et al. (2018) and make no assumptions about splay faulting. It is important to note that we do not choose to follow the Gutenberg-Richter relationship for probabilistic hazard analysis, as we are exploring the range of possible tsunami inundation behaviors from various heterogeneous sources. Finally, we calculate the "pseudo-vertical" coseismic deformation for each rupture model, which we use as the initial condition for tsunami modeling.

2.2 Tsunami modeling

The coseismic deformation is obtained by combining the vertical displacement from elastic dislocation with the "pseudo-vertical" response from horizontal displacement of sloping bathymetry (Tanioka et al., 1997). We do not consider secondary sources of tsunamigensis, such as submarine landslides, splay faulting, or plastic deformation of the shallow wedge in the tsunami initial condition. These quantities — though they do contribute to total tsunami energy and increased tsunami amplitudes (Ma and Nie, 2019) — are difficult to systemically and stochastically model. Thus, underestimation of tsunami amplitudes and inundation from each of these sources may be likely should they occur locally near any of the three areas of interest.

Following the definition of the initial tsunami condition, we use the finite volume depth-averaged tsunami modeling code GeoClaw (Clawpack Development Team, 2020). It can numerically solve the two-dimensional nonlinear shallow water equations. It utilizes adaptive mesh refinement (AMR) such that areas of large tsunami complexity are automatically refined to higher discretization levels. The model domain is shown as the extent of Figure 2. For propagation in the open ocean, we use SRTM15, which provides bathymetry and topography at 15 arcsec resolution (Tozer et al., 2019), which is what we use for AMR levels 1-3. We interpolate up from the 1/9 arcsec provided by continuously updated digital elevation model (CUDEM) at mean high water for Ocean Shores, WA and Newport, OR to 1/3 arcsec (Cooperative Institute for Research in Environmental Sciences). We do nothing to the 1/3 arcsec mean high water digital elevation model (DEM) for Crescent City, CA (NOAA National Geophysical Data Center). These 1/3 arcsec grids are then used for our finest discretization and for our inundation regions. Lastly, we permit inundation up to elevations of 80 m above mean high water. We recognize that this value is two times higher than the maximum inundation surveyed from the Tohoku-Oki tsunami (Mori et al., 2011); however, our focus is to examine all potential inundation behaviors.

We run the tsunami models for 2 hours of model time. This choice of run time means that reflections from distant features and long-term edge waves are not considered. Time-stepping is allowed to vary such that the Courant- Friedrich-Levy condition stays at a constant 0.75. For tsunami inundation, we employ a Manning coefficient of 0.025 (which is uniform over the entire spatial domain), and we utilize the drying and wetting feature of GeoClaw to allow changes to our grid cells as the simulation progresses. We realize that a spatially uniform Manning coefficient is not compliant to the methods used by the ASCE, as spatially varying Manning coefficients require knowledge of the land use footprint of the sites, which is currently unavailable.

We assume that, because rupture velocities are faster than the tsunami wave velocities, instantaneous coseismic deformation for the tsunami initial condition is a valid approximation. This has been shown to be true for near-shore tsunami amplitudes (Williamson et al., 2019).

2.3 Comparisons of hazards between homogeneous and heterogeneous ruptures

Although we make use of some of the concepts behind probabilistic tsunami hazard analysis (PTHA) framework for inundation, we note that the results below do not constitute a formal PTHA assessment. Merely, we are interested in ascertaining the uncertainty of inundation that is introduced from utilizing homogeneous versus heterogeneous earthquake sources for the CSZ. We are not assuming a particular Gutenberg-Richer distribution or a characteristic earthquake return period, as required by a true PTHA for the region. We operate on the assumption that each rupture that falls in to either the L-like or XL-like class and has either a 1-in-3,333-year or 1-in-5000-year chance of occurring during a year. Witter et al. (2011), Goldfinger et al. (2012), and Witter et al. (2013) find that there is evidence for 3 L class ruptures over the 10,000 years of paleoseismic and turbidite records, giving the probability of 1-in-3,333-years. They also find evidence for 1 XL/XXL class rupture, giving a probability of 1-in-5,000-years. We understand that this method of annual probability is an oversimplification and neglects information about the earthquake cycle. However, that is how the annual probabilities have been determined by the various USPNW agencies (Witter et al., 2011; Eungard et al., 2018).

We create maps showing the spatial differences of inundation limit for the three sites. We compare the results of the heterogeneous L-like and XL-like particles to their respective deterministic, homogeneous scenarios. We take the mean of each individual grid cell for the 100 particles of the L-like and XL-like particles and convert them into geospatial raster files. We assert that grid cells having a mean inundation depth of ≥ 0.3 m are "wet" and that grid cells below this threshold are "dry." This threshold is introduced to remove the effects of extreme events that skew the mean behavior of inun-

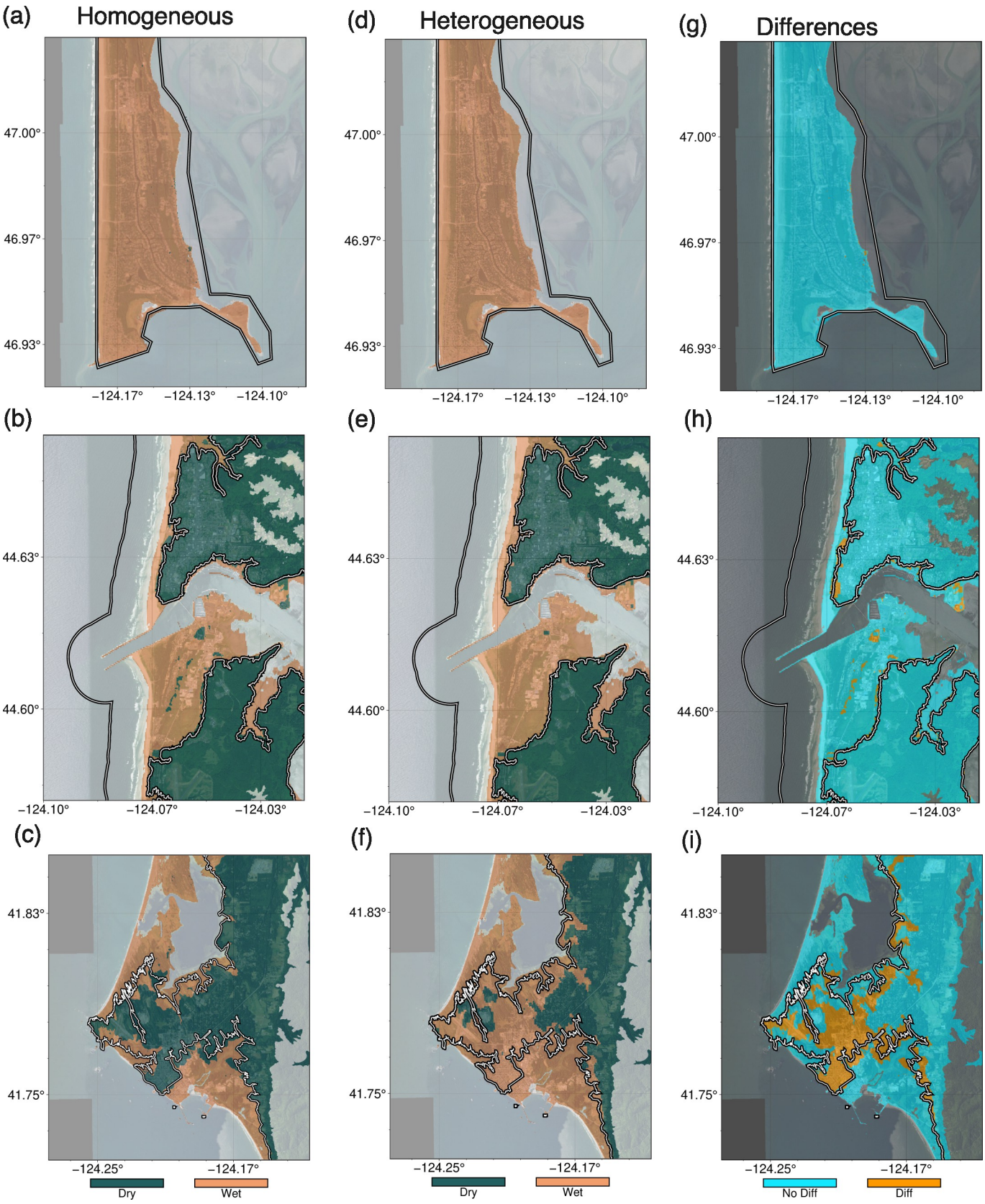

Figure 4 The mean of each individual grid cell for the 100 L-like scenarios (or particles). (a),(b),(c) The L1 homogeneous, deterministic model run where inundation limit is defined by "wet" grid cells where inundation is $\geq$ 30 cm and "dry" where inundation $<$ 30 cm. (d),(e),(f) Similar to (a)-(c) except the inundation limit is defined by the average of 100 L-like particles. (g),(h),(i) the differences between "wet" and "dry" grid cells of (a)-(c) and (d)-(f) for Ocean Shores, WA; Newport, OR; and Crescent City, CA. Black lines denote the official tsunami evacuation lines used for by the states of Washington, Oregon, and California (State of Oregon, 2024; State of California, 2022). These maps were constructed using GMT 6 (Wessel et al., 2019).

dated grid cells. We utilize the Jaccard similarity index (JSI) for computing the similarity between the homogeneous raster files and the L-like and XL-like heterogeneous rupture mean inundation limit raster datasets (Jaccard, 1912). JSI values range from $0-1$, with 0 indicating no overlap between datasets and 1 indicating a perfect match.

While the aforementioned method illuminates the varying inundation limit behaviors of heterogeneous particles, it does not provide a robust statistical measure and serves as a first step. Therefore, we compute the mean inundation depth for all inundated cells for each heterogeneous particle and display them as violin plots. That is take every grid cell that is inundated for each particle and calculate the mean inundation depth of only the inundated grid cells. We compile the hazard curves for all inundation-allowable grid cells. We use the nearest quarter percentile of the L-like particles to plot the inundation limits from the associated hazard curves, and we utilize a similar approach for the 50$^{\text{th}}$ percentile for the XL-like particles. We then assign inundation probabilities to the grid cells. We note that for the hazard curves geospatial datasets, we show the three sites without deformation. This detail is to keep our results inline with ASCE 7-22. For the comparisons of deterministic scenarios to the L-like and XL-like particles, we show the results with deformation, as they become important for showing the differences between particle statistics.

Rather than use the PTHA equation formulated by Geist and Parsons (2006), we adopt a simpler probabilistic equation. Suppose we have events $E_1, E_2, E_3, ..., E_k$ each with an annual probability p_k, and since each realization is an independent event, we can produce the following equation:

$$\hat{p} = 1 - (1 - p_1)(1 - p_2)...(1 - p_k), \tag{1}$$

Where $\hat{p}$ is the probability that at least one of the events happens. From this equation, we can show that for any exceedance value h, the probability $P(h)$ that inundation occurs at a point on the grid for events E_k where $h_k > h$ becomes:

$$P(h) = 1 - (1 - p_1)...(1 - p_n), \tag{2}$$

where n is the number of times the grid point is inundated. n can be less than or equal to the total number of events k. From these equations we are able to produce hazard curves and maps for each of our three sites of interest. In addition to these maps, we construct violin plots that show the probability distribution function of the mean for all grid points that are inundated by each rupture scenario. Violin plots show the breakdown of inundation behavior by geodetic model and by the total of all models (Figure 7).

We create inundation limit maps that show the probability of inundation exceedance above 0 m. We set only one exceedance boundary: 0.004 ($\sim$ 1-in-2,475-years). This boundary is of interest since it is the standard by which USPNW states determine the tsunami design zone boundaries (American Society of Civil Engineers, 2022). We compare our results to the official tsunami evacuation lines used by Washington, Oregon, and California and the tsunami design zone as determined by the ASCE 7-22 framework.

2.4 Restatement of methods by analogy

We explain this method in simpler terms by drawing analogies to the field of atmospheric science and meteorology, in particular data assimilation. The process of making a useful weather forecast depends on the climatology (i.e., previous model behavior), which is usually done by running the weather model for 1-2 weeks or longer of simulation time (Van Leeuwen, 2009). These models have a well defined knowledge of the synoptic governing equations. This is not the case for earthquakes. For the CSZ, we assume that we do not know its "climatological" behavior. We make the assumption that this "climatological" behavior follow one of four geodetic locking models. We generate 25 scenarios (or particles as they are referred to in meteorology and data assimilation literature) to represent 83,000 years (L-like) - 125,000 years (XL-like) of "climatology" per geodetic locking model, and we assert that they either fall into an L-like or XL-like behavior. Again, L-like and XL-like refer to the arbitrary choice of moment magnitude bins described by Witter et al. (2011) and Witter et al. (2013). We run these particles to then get the statistics of inundation, which have been the previous subsections.

We then compare these particle statistics to the deterministic model runs of the L1 and XL1 "t-shirt" models. By not committing to a formal PTHA analysis, we allow our results to stay general enough to be transformed into a Bayesian framework (Van Leeuwen, 2009). Although, we do not commit to this here. Instead, we show how to generate the particle statistics for inundation and how they may be of use for different stakeholders.

3 Results

We start our analysis by investigating the spatial variations in inundation limit between the homogeneous and heterogeneous source models and particles. We then calculate the mean inundation depth percentiles for the two rupture classes. Next, we utilize these percentiles to show the inundation limit uncertainties when using hazard curves. Lastly, we show the inundation limits when accounting for the MRP of the stochastic particles.

3.1 Differences between homogeneous and heterogeneous ruptures.

Figure 4 shows the difference between the L1 source rupture model and the L-like heterogeneous particles. Grid cells are considered "dry" if the mean inundation depth is $<$ 30 cm and "wet" if $\geq$ 30 cm. We see that for Ocean Shores that the there are none-to-few pockets of "dry" grid cells from the L1 model on the southern and eastern extents of the peninsula. With the L-like heterogeneous particles, the entirety of Ocean Shores is "wet." The JSI for Ocean Shores is 0.99 (Table 1), indicating

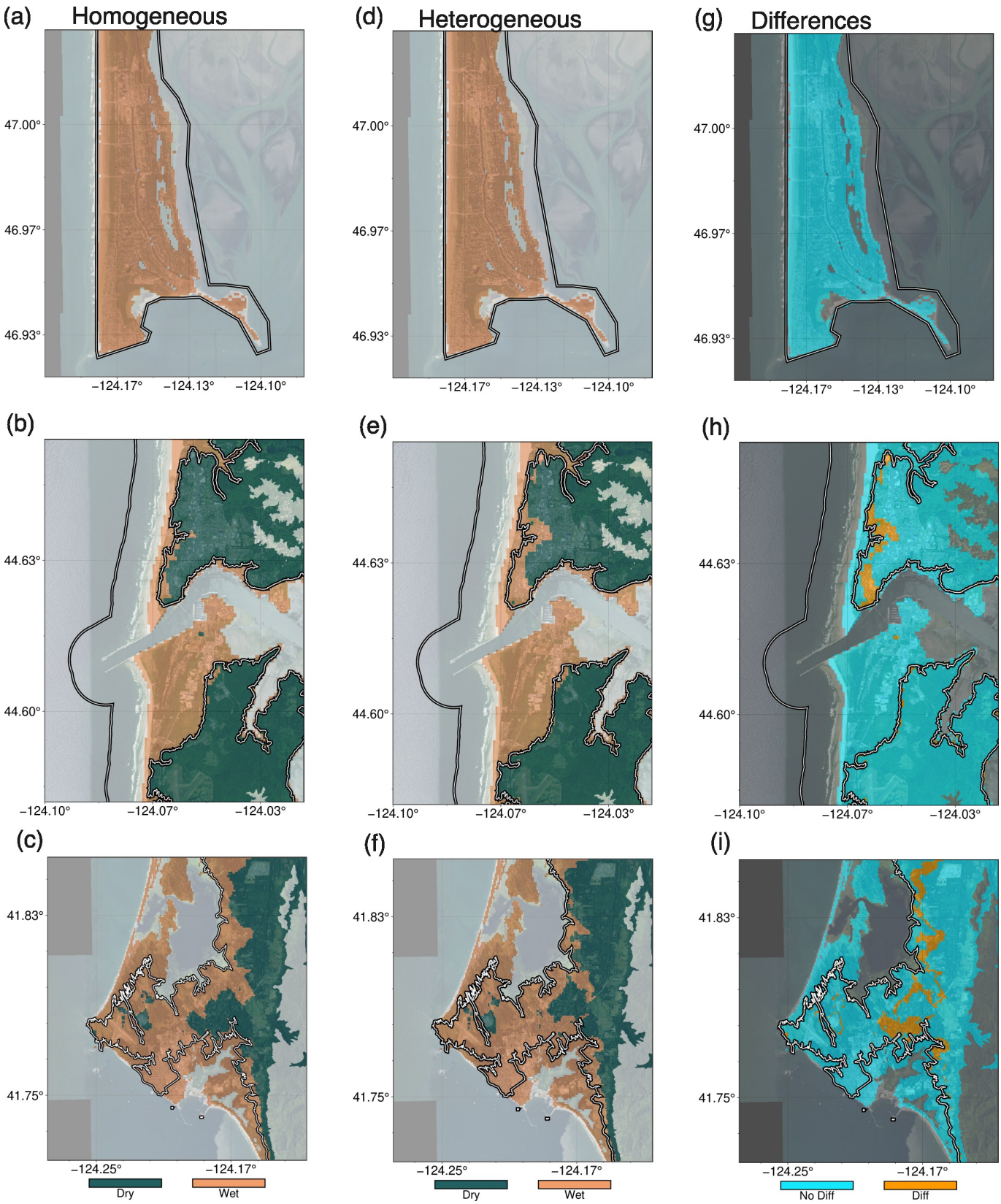

Figure 5 The mean of each individual grid cell for the 100 XL-like scenarios (or particles).(a),(b),(c) The XL1 homogeneous, deterministic model run where inundation limit is defined by "wet" grid cells where inundation is $\geq$ 30 cm and "dry" where inundation $<$ 30 cm. (d),(e),(f) Similar to (a)-(c) except the inundation limit is defined by the average of 100 XL-like particles. (g),(h),(i) the differences between "wet" and "dry" grid cells of (a)-(c) and (d)-(f) for Ocean Shores, WA; Newport, OR; and Crescent City, CA. Black lines denote the official tsunami evacuation lines used for by the states of Washington, Oregon, and California (State of Oregon, 2024; State of California, 2022). These maps were constructed using GMT 6 (Wessel et al., 2019).

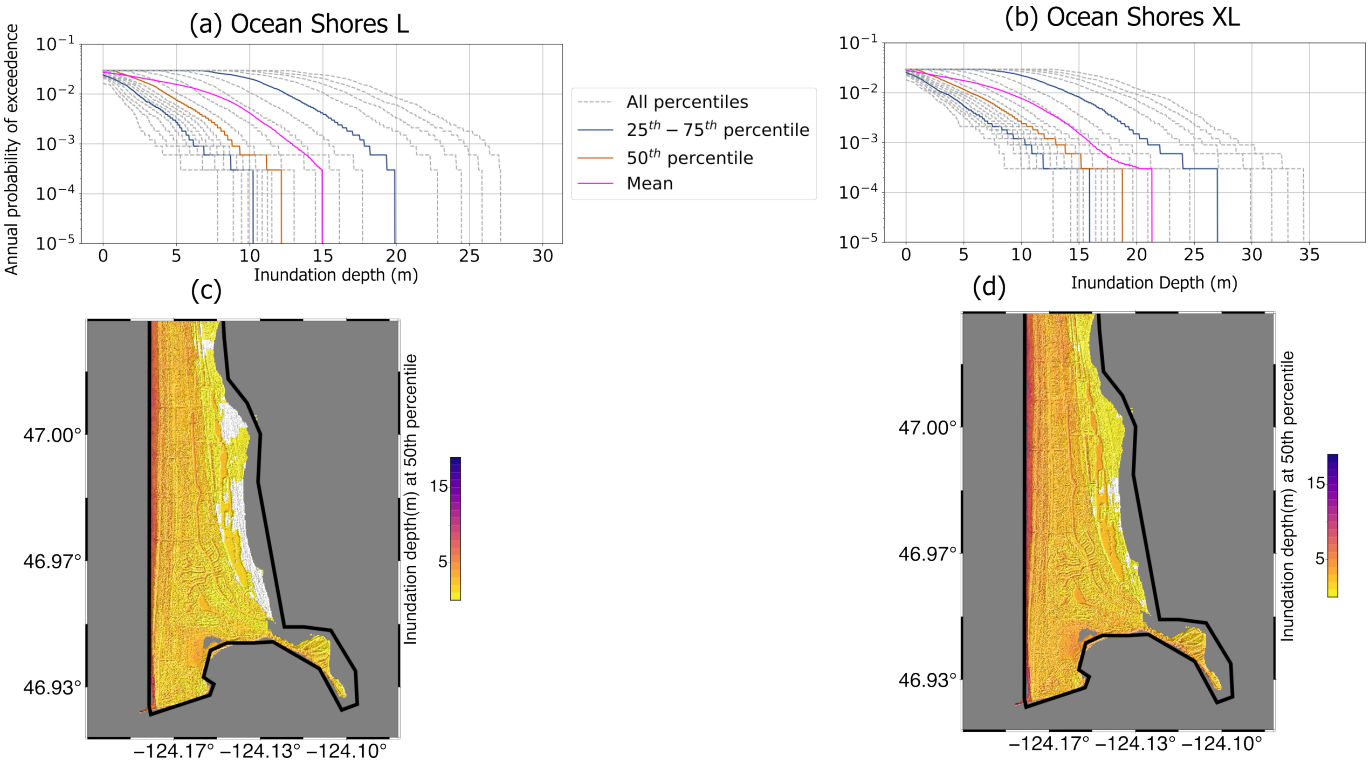

Figure 6 (a) Hazard curves for all grid cells that inundate for the 100 L-like heterogeneous particles at Ocean Shores, WA. (b) Same as (a) but for 100 XL-like heterogeneous particles. (c) The inundation limit of the 100 L-like heterogeneous particles at the 50th percentile. (d) The inundation limit of the 100 XL-like heterogeneous particles at the 50th percentile. Black lines in (c) and (d) is area within the official tsunami evacuation zone. These maps were constructed using GMT 6 (Wessel et al., 2019).

Site	L-like (0-1)	XL-like (0-1)
Ocean Shores	0.99	1
Newport	0.97	0.96
Crescent City	0.81	0.94

Table 1 Jaccard similarity indices of Ocean Shores, Newport, and Crescent City for similarity between the homogeneous and heterogeneous spatial rasters of "wet" and "dry" tsunami inundation.

the homogeneous and heterogeneous scenario and particles cause tsunami inundation that are about similar. In the case of Newport, we see the largest differences in North Newport (Figure 4). The L1 scenario fails to inundate past the beach areas; however, the L-like heterogeneous particles are able to inundate up to the tsunami evacuation line, whose inundation limit is determined by the XXL1 scenario (Witter et al., 2013). South Newport, which has steep topographic variations, does not see as many differences. This reflects in the overall JSI of 0.97 (Table 1). Crescent City is the site with the largest differences between the homogeneous L1 and heterogeneous L-like particles with a JSI of 0.81 (Table 1). In this case, all of downtown Crescent City is inundated with only the central area remaining "dry."

Figure 5 shows the differences between the XL1 source rupture model and the XL-like heterogeneous particles. In this case, there is no difference in "wet" and "dry" inundation limit for Ocean Shores. The JSI is 1 — a perfect match (Table 1). For Newport, the majority of differences between the homogeneous and heterogeneous cases continues to be in North Newport (Figure 5 inset). The inundation limit can be at widest 600 m further inland than the XL1 case. The JSI are 0.96, which indicates a greater similarity between the spatial extents of "wet"/"dry" behavior of the homogeneous and heterogeneous ruptures; however, the majority of differences are in locations of non-negligible population density (Table 1 and Figure 5). Crescent City continues to see a large horizontal extent of the inundation limits with both XL homogeneous and heterogeneous model and particles. The difference between the two being mostly in the total coverage of "wet" cells in the center of Figure 5i. The JSI is 0.94 indicating that the two are roughly similar to each other; however, again, the differences appear to be in areas of non-negligible population density (Table 1 and Figure 5).

3.2 Mean inundation behavior

Figure 7 shows the probability distribution of the mean tsunami inundation behavior for all three sites of interest based on the rupture models. These plots show the probability distribution of the mean of all inundated grid cells for the particles by geodetic locking models compared to the mean of all inundated grid cells of the deterministic model runs. There does not appear to be a correlation between geodetic locking models and inundation impacts (Figure 7). What is clear is that, compared to the inundation from heterogeneous particles, the L1 model consistently ranks between the 45th - 75th percentiles of for Ocean Shores and Newport. Crescent City has the L1 mean inundation depth

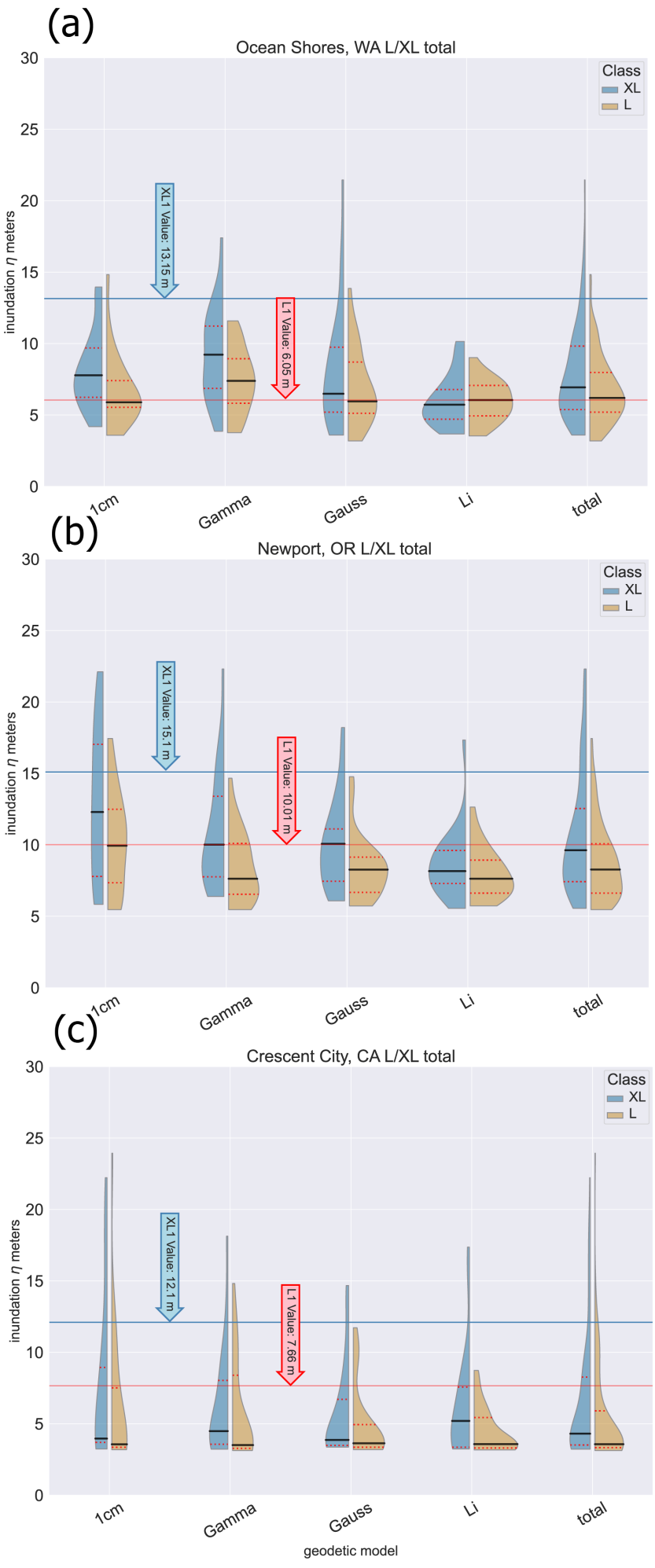
(a)
Ocean Shores, WA L/XL total
Class
XL
L
XL1 Value: 13.15 m
L1 Value: 6.05 m
inundation η meters
0
5
10
15
20
25
30
1cm
Gamma
Gauss
Li
total
(b)
Newport, OR L/XL total
Class
XL
L
XL1 Value: 15.1 m
L1 Value: 10.01 m
inundation η meters
0
5
10
15
20
25
30
1cm
Gamma
Gauss
Li
total
(c)
Crescent City, CA L/XL total
Class
XL
L
XL1 Value: 12.1 m
L1 Value: 7.66 m
inundation η meters
0
5
10
15
20
25
30
1cm
Gamma
Gauss
Li
total
geodetic model

Figure 7 (previous page) Violin plots of the mean tsunami inundation behavior for each geodetic model and all models. Probability distribution functions shows distribution of the mean of all inundated cells for each particle (see Figures 4 and 5 for approximate inundated cell extent). We restate that is taking every grid cell that is inundated for each particle and calculate the mean inundation depth of only the inundated grid cells. Red dashed lines delineate the 25th and 75th percentiles. Solid black lines delineates the 50th percentile. Blue line and arrow show the mean value of all inundated grid cells for the XL1 scenario. Likewise, red line and arrow show the mean value of all inundated grid cells for the L1 scenario. Violin plots are shown for (a) Ocean Shores, WA; (b) Newport, OR; and (c) Crescent City, CA.

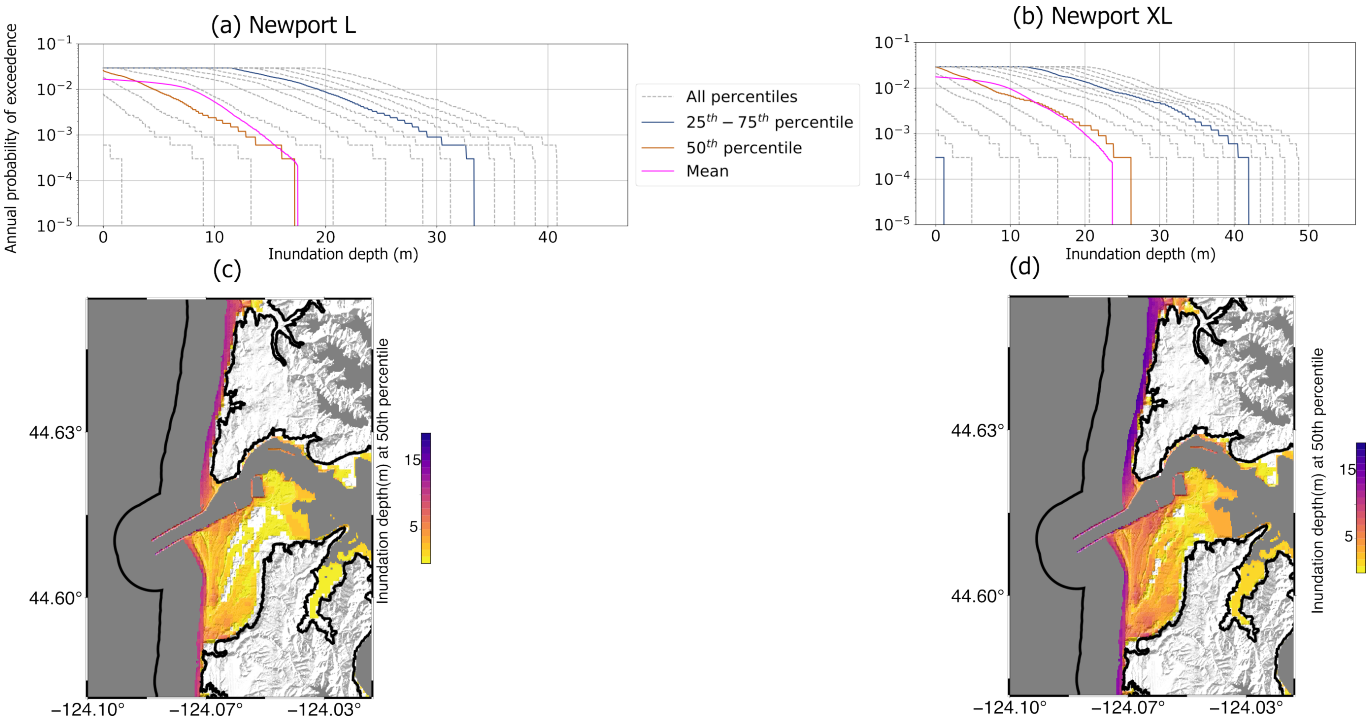

Figure 8 (a) Hazard curves for all grid cells that inundate for the 100 L-like heterogeneous particles at Newport, OR. (b) Same as (a) but for 100 XL-like heterogeneous particles. (c) The inundation limit of the 100 L-like heterogeneous sources at the 50th percentile. (d) The inundation limit of the 100 XL-like heterogeneous particles at the 50th percentile. Black lines in (c) and (d) is area within the official tsunami evacuation zone (State of Oregon, 2024). These maps were constructed using GMT 6 (Wessel et al., 2019).

at the 75th percentile. Overall, this behavior means that the L1 scenario represents only the median to 75th percentile behavior that can be expected from heterogeneous particles. The XL1 scenario consistently ranks $>$ the 90th percentile for all geodetic families and even in the total. The XL1 scenario thereby represents an extreme scenario, closer to what an MCE ought to be, with its average of all inundated points being between 12-15 m among the three sites of interest. Our comparisons of inundation limit for the L-like particles from the hazard curves are performed at the 50th percentile for Ocean Shores and Newport; meanwhile, Crescent City's inundation limit is shown at the 75th percentile. All three sites have their inundation limits examined at the 95th percentile for comparisons of the XL-like particles. While Figure 7 shows a top-level view of tsunami inundation depth behavior, it neglects to account for the spatial variability of inundation limits. Figures 6 — 9 show this for the L-like particles at the median percentile for Ocean Shores, Newport, and Crescent City determined by their associated hazard curves. We see from Figures 6(a), 8(a) and 9(a) that the hazard curve uncertainty is greatest for Newport and Crescent City and smallest for Ocean Shores. Pockets of low inundation depth at the 50th percentile are noticeable for Ocean Shores, especially on the bay side section of the peninsula, which may suggest little to no inundation in those regions for L-like particles that follow median behavior. Newport's inundation limit and inundation depth at the 50th percentile are more in line with the L1 inundation limit and inundation depth (Figures 8(c) and 4(b)), despite the large uncertainties indicated by its hazard curves. Crescent City best illuminates the large uncertainty indicated by the hazard curves (Figure 9(a)). The inundation depth is ≤ 1 m, and its inundation limit does not extend far into the evacuation zone. Indeed, the inundation limit at the median percentile would be a best case scenario for the town.

Figures 6(d), 8(d) and 9(d) show the inundation limit of the XL-like particles at the 50th percentile. This percentile was selected to better compare the quasi-homogeneous XL1 scenario and our heterogeneous particles. Aside from Ocean Shores, which always inundates in this class, Newport has inundation limits that extend past their official tsunami evacuation lines. Crescent City has its evacuation lines constraining the

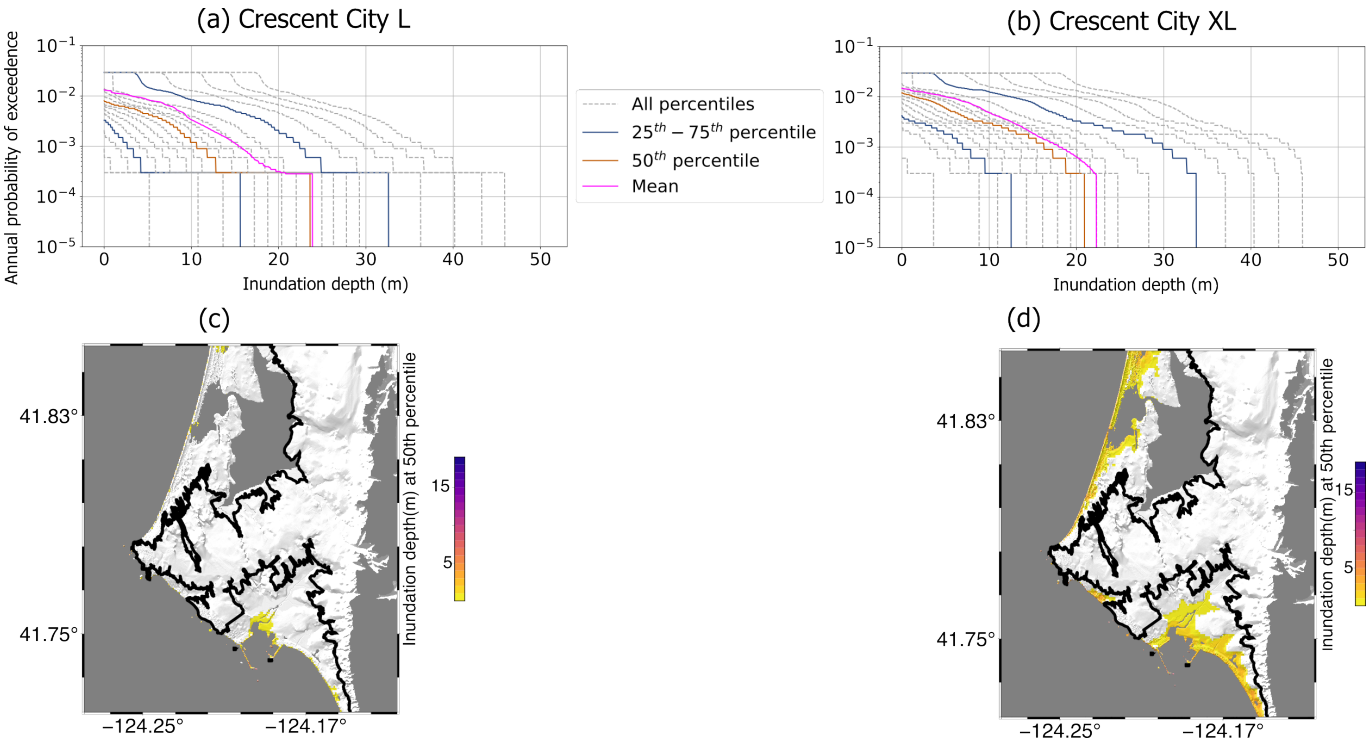

Figure 9 (a) Hazard curves for all grid cells that inundate for the 100 L-like heterogeneous particles at Crescent City, CA. (b) Same as (a) but for 100 XL-like heterogeneous particles. (c) The inundation limit of the 100 L-like heterogeneous particles at the 50th percentile. (d) The inundation limit of the 100 XL-like heterogeneous particles at the 50th percentile. Black line in (c) and white line in (d) are the areas within the official tsunami evacuation zone (State of California, 2022). These maps were constructed using GMT 6 (Wessel et al., 2019).

inundation limit of the XL-like particles. While the uncertainty associated with these results is still considerable given their hazard curves (Figures 8(b) and 9(b)), they are less uncertain than the L-like particles. Inundation depths at the 50th percentile are > 5 m; however, Newport's inundation depths are most extreme on the beach areas. Meanwhile, Crescent City experiences a better outcome. We highlight that for calculation and display of the hazard curves, we neglect to show the average deformation of the heterogeneous particles, which manifests as subsidence at all sites. This subsidence permits inundation to extend further inland than considered by the official tsunami evacuation lines. Although, this result would seem to indicate a best case scenario, we show in the next section that this inundation limit is outside the 1-in-2475-year exceedance limit that would be considered by the ASCE 7-22 guidelines.

3.3 Maximum considered tsunami inundation limit

When we plot the inundation limit of the two classes against the tsunami evacuation and ASCE 7-22 tsunami design zone boundaries for the three sites of interest with the probability of inundation ≥ 0 cm at a 1-in-2475-year exceedance, we see the limits of using homogeneous source models as the basis for an MCT. As seen in Figures 10 and 11, North Newport's tsunami evacuation lines, which are set to the XXL1 scenario, can have its inundation limit met or exceeded by L-like and XL-like heterogeneous particles. However, areas with steeper variations of topography constrain inundation limit similar to the DOGAMI evacuation lines. Crescent City, which uses a 1-in-975-year MRP event inundation limit, fails to encapsulate the inundation limit for the L-like and XL-like particles. Indeed, the ASCE 7-22 tsunami design zone departs from the inundation limit of the official tsunami evacuation lines. Moreover, one thing is clear, heterogeneous sources with the exceedance threshold being considered by USPNW states and engineers have inundation limits that extend further inland than their respective homogeneous events' inundation limits.

4 Discussion

The primary focus of this study is to compare between homogeneous and heterogeneous earthquake sources to be used as the tsunami initial condition for inundation at three sites of interest. Our results have shown that while the XL1 scenario represents an extreme case with its inundation depth, its inundation limit is less than that of the heterogeneous particles. Indeed, we find that heterogeneous sources have inundation limits that exceed the official tsunami evacuation lines, which are based on various homogeneous source models. We discuss the implications of this result below.

4.1 Differences beween homogeneous and heterogeneous models

The XL1 scenario produces large inundation depths on average for all of the grid cells it inundates across the three sites. However, the horizontal inundation

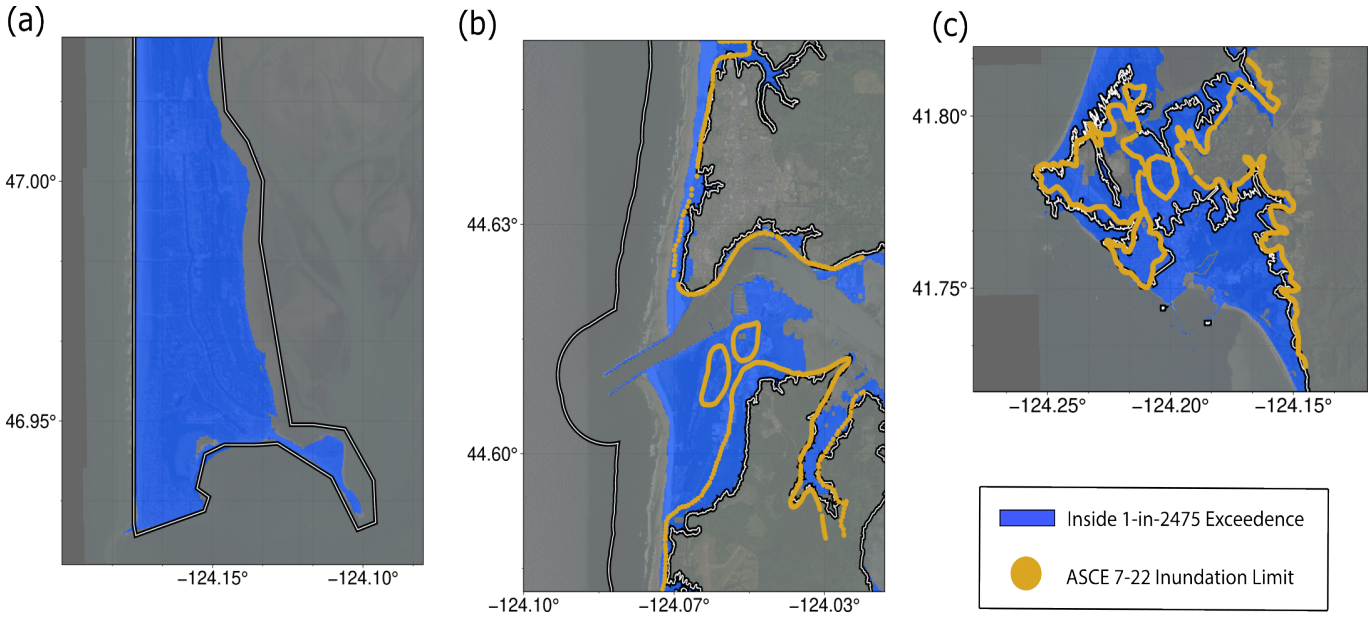

Figure 10 Maps that show the 1-in-2475-year exceedance inundation limit for the L-like heterogeneous particles for (a) Ocean Shores, WA; (b) Newport, OR; and (c) Crescent City, CA. Goldenrod circles denote the inundation limit from the American Society of Civil Engineers (American Society of Civil Engineers, 2022). Ocean Shores is entirely within the tsunami design zone, so the goldenrod circles do not appear in the figure. Official tsunami evacuation zones are shown in black (a),(b), and(c) (State of Oregon, 2024; State of California, 2022). These maps were constructed using GMT 6 (Wessel et al., 2019).

limit is less than the mean behavior of the heterogeneous sources. There are two proposed drivers of increased horizontal inundation limit: (1) source complexity in the near-trench zone and (2) local coseismic subsidence.

Small and Melgar (2021) showed that high slip deficits in coupling lead to frequent high slip in stochastically generated events. These areas of high slip tend to happen more in the near-trench area for the 1 cm/yr and Gamma models, thereby producing more particles with higher tsunamigenic potential. This correlation is not seen in Figure 7 at any of the sites. Indeed, higher tsunamigenic potential in local and regional scales has been shown to be more a function of near-trench locking behavior. However, this fact alone does not explain the further horizontal extent of inundation limit at the three sites compared to the homogeneous scenarios.

All of these rupture families are more likely to produce coseismic coastal subsidence than coastal uplift, which is widely believed to have occurred during the previous ∼M9 event in 1700 (Witter et al., 2013; Melgar, 2021; Walton et al., 2021). Coseismic coastal subsidence allows for more area to be below mean high water thereby allowing for tsunami waves to inundate further inland. This manifests in the XL1 scenario for Ocean Shores and Crescent City (Figure 5). Heterogeneous sources of L- and XL-like categories also produce various amounts of coseismic coastal subsidence. It can be so severe that entire sites of interest can be fully below mean high water before the first tsunami wave arrives. The only site that did not have this event occur was Newport, which only saw modest coastal coseismic subsidence of 0-8 m for the 200 rupture particles. Due to the source complexity of these particles, it was common for the two out of the three sites farthest from the main rupture asperity to have inundation depths of 0-3 m while the other site local to the main asperity had inundation depths of 10-20 m. This behavior was seen in the 2011 Tohoku-Oki tsunami wherein local tsunami runup was > 40 m for places near the main rupture asperity (Mori et al., 2011, 2022). Indeed, our results indicate that local coseismic subsidence nearest the main heterogenic rupture asperity causes these extreme inundation depths and horizontal inundation limits. This type of inundation behavior is difficult to replicate with homogeneous and quasi-homogeneous ruptures.

The ASCE 7-22 tsunami inundation model appears to further inundate Crescent City compared to the official tsunami evacuation lines (see ASCE 7 Tsunami-Database, Figures 10 and 11). Their model makes use of the 1 cm/yr and top of the non-volcanic tremor zone geodetic models (American Society of Civil Engineers, 2022). The latter of which has been shown by Small and Melgar (2021) to produce substantial coastal coseismic uplift to the point that it represents a much less likely scenario. The ASCE 7-22 codes only assign a probability of 0.3 to this model; however, as we have shown, coastal coseismic subsidence is the primary driver of increased horizontal inundation limits for the site. Increased research should be undertaken to validate the use of the top of the non-volcanic tremor zone for PTHA, as its inclusion may potentially cause underestimation of the horizontal inundation limit at Crescent City.

Another driver of increased horizontal inundation limits is terrain flatness. Although this fact is widely known (Mori et al., 2022), our study highlights that combined with the other drivers, it can cause greater uncertainty. For example, Ocean Shores is entirely flat, and its hazard curves (Figure 6(a, b)) reflect this fact with lower uncertainty. Newport, which has steeper to-

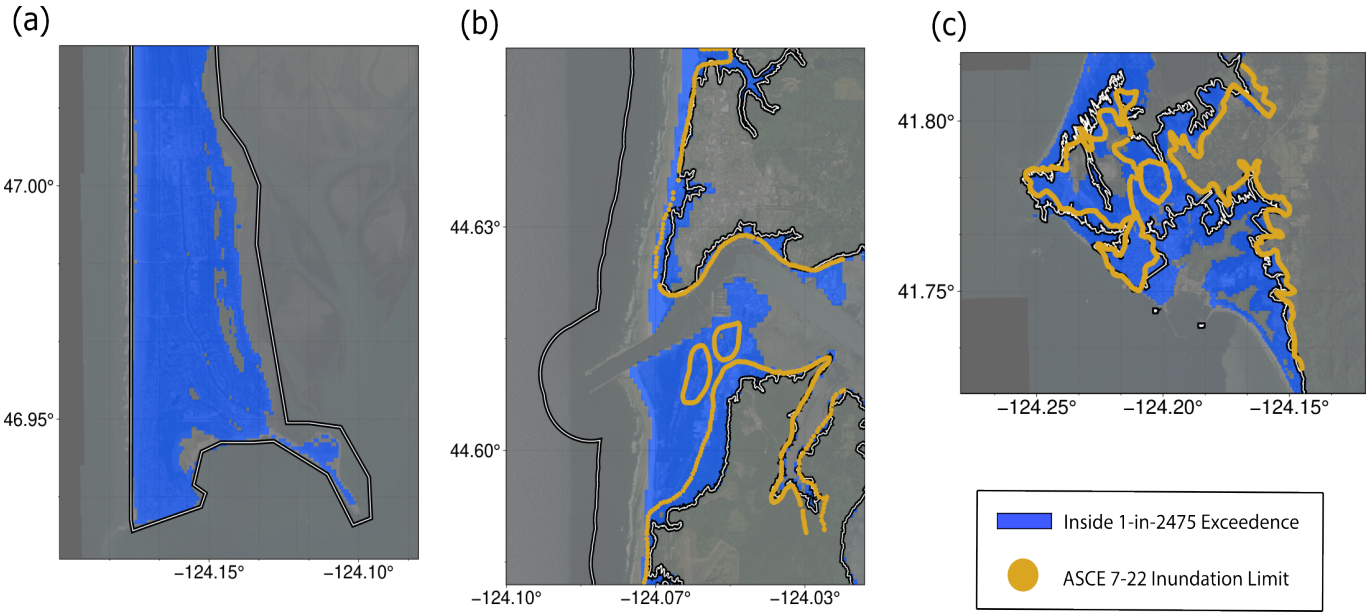

Figure 11 Maps that show the 1-in-2475-year exceedance inundation limit for the XL-like heterogeneous particles for (a) Ocean Shores, WA; (b) Newport, OR; and (c) Crescent City, CA. Goldenrod circles denote the inundation limit from the American Society of Civil Engineers (American Society of Civil Engineers, 2022). Ocean Shores is entirely within the tsunami design zone, so the goldenrod circles do not appear in the figure. Official tsunami evacuation zones are shown in black (a),(b), and (c) (State of Oregon, 2024; State of California, 2022). These maps were constructed using GMT 6 (Wessel et al., 2019).

pographic variations, shows that uncertainty increases when the area is a mix of flat and steep topography (Figure 8 (a,b)), especially when the elevation of the topography remains much higher than the local coseismic subsidence. Crescent City is a mix of the two topographic behaviors; however, its topographic elevation is only slightly greater than the local coseismic subsidence at higher percentiles. The elevation of Crescent City above mean high water can be 10-30 m north of the harbor and between Lake Earl, with elevations quickly rising to ≥ 80 m on the east side of town. This fact highlights why inundation depths and inundation limit are small when the main rupture asperity is far from the area. However, it highlights why the area is more vulnerable if the main asperity is near to it.

4.2 Limitations of this work

New breakthroughs in understanding the CSZ seismogenic properties are happening at a rapid pace with the advent of the first CAscadia Seismic Imaging Experiment 2021 (CASIE21) papers being published (Carbotte et al., 2024; Ledeczi et al., 2024). One of the more consequential findings being that the mega-splay used for scenario "1" of the "t-shirt" scenarios likely does not contribute much, if at all, to the tsunamigenic potential of the CSZ (Carbotte et al., 2024; Ledeczi et al., 2024). The mega-splay is the chief contributor to the horizontal extent of the inundation limit seen in Washington and Oregon. However, we have shown that the inundation limit from mega-splay rupture can be met and exceeded with stochastic and heterogeneous ruptures. We posit that the similarity between our results and those of the mega-splay are tied to the terrain factors as mentioned in the previous section.

One of the implicit assumptions of this work is the assumption of bare earth digital elevation models. Anthropogenic factors are not considered; although, they have been shown to influence the properties of tsunami flow that cause large deviations from expected behavior (Mori et al., 2022). One of these factors, the Manning coefficient, can change widely as a result of land use properties (Koshimura et al., 2009; Takagi and Bricker, 2014). However, we maintain that it must be spatially uniform throughout our simulations at 0.025. The ASCE 7-22 guidelines for the Manning coefficient are 0.025-0.03 for coastal water nearshore bottom friction, 0.025 for open field/land, 0.04 for buildings of at least urban density, and 0.03 for all other cases (American Society of Civil Engineers, 2022). The consequence being that our inundation limit can extend further inland compared to the ASCE, as we assume that our sites are all just open land/fields. Indeed, future research directions must address this issue. We neglect it since the science of constraining the Manning coefficient in the anthropogenic environment is still in its infancy (Mori et al., 2022). For example, it has been shown that the Manning coefficient can change as a function of water column load as shown by Boyer (1954), where it can be as high as 0.075. Although we potentially overestimate the flood limit by 20- 60% in urban areas compared to the ASCE 7-22 guidelines.

ASCE 7-22 sets an artificial cap on the Manning coefficient, as it neglects the works of Takagi and Bricker (2014) and Koshimura et al. (2009). These papers find that Manning coefficients approach 0.2, when tsunami flow is laden with debris, which is much larger than the artificial cap of 0.04 recommended by the ASCE's Tsunami Loads and Effects Subcommittee. That is mostly the result of their Manning coefficient's being derived from land use laboratory experiments.

Whereas in Koshimura et al. (2009) and Takagi and Bricker (2014), Manning coefficients are derived from real world damage data.

4.3 Use the "t-shirt" models to convey tsunami hazards to the public

For two of the three sites of interest, the exceedance maps that consider fully heterogenous slip do not differ much from the official tsunami evacuation lines used by their state emergency planners. WaDNR and DOGAMI have done extensive research preparing for the next CSZ event, and it is reflected in the similarity of the tsunami evacuation lines to even the XL-like heterogeneous ruptures. Only Crescent City does not have tsunami evacuation lines — at the present moment — that encapsulate the risks of homogeneous or heterogeneous ruptures of the CSZ. Even ASCE 7-22 goes further inland with its tsunami runup elevation than the results used by California (American Society of Civil Engineers, 2022). Although the departures from the official tsunami evacuation lines for Crescent City are large, it is important to remember that their lines were chosen for a 975-year scenario with a safety factor included and that their evacuation lines were made with community involvement. While our work may indicate that a future CSZ tsunami can inundate further inland, the ruptures utilized are simply an exploratory set that does not make use of the USGS Powell Center's CSZ logic tree. The tsunami evacuation lines must be made with the utmost care due to the psychological and economic impact they can have on people who live and visit these communities. The scientific and engineering communities embrace a probabilistic framework for approaching the next CSZ earthquake and tsunami, and the aleatory and epistemic uncertainties that accompany it. However, this framework neglects the emergency offices' need for deterministic-like events to convey the threat to their communities. Perhaps the biggest consequence of this work, despite its drawbacks, is that stochastically generated heterogeneous ruptures can match and exceed the inundation limits of the L1 and XL1 "t-shirt" models in exceedingly rare events. Our use of a consistent Manning coefficient of 0.025 means that we potentially overestimate the inundation limit by 20-60% in urban areas compared to the ASCE 7-22 guidelines, which would have our results be constrained by the XL1 and XXL1 "t-shirt" models. Emergency managers could continue to use DOGAMI "t-shirt" models to communicate the best evacuation strategies for their communities. Meanwhile, they can utilize the probabilistic nature of the upcoming PTHA changes to make their communities more resilient to the hazards of the CSZ. The various USPNW state legislatures are in the process of ratifying new building codes that choose an MCT of 1-in-2,475-year MRP. It is imperative that this reference event contain the best knowledge of the tsunami inundation behavior if substantial casualties are to be avoided in the next CSZ rupture. Although, they must come to terms that each great earthquake rupture is different, and that building in the currently known tsunami inundation zone is a dangerous task.

5 Conclusion

We have shown the range of tsunami inundation behaviors from 200 stochastically generated heterogenic rupture scenarios (or particles) for the sites of Ocean Shores, WA; Newport, OR; and Crescent City, CA. We find that while homogeneous scenarios have mean tsunami inundation values between the 45^{th}-75^{th} percentiles (L1) and the > 90th percentile (XL1), the L-like and XL-like heterogenic sources have a greater inundation limit. This larger spatial extent is well-constrained by the tsunami evacuation lines of Ocean Shores and Newport. However, Crescent City's lines fail to account for the greater spatial extent of both homogeneous and heterogeneous rupture sources. We suggest that emergency managers continue the use of the XL / XXL1 scenarios to communicate the risk of hazards to their communities. Our proposed inundation limits are overestimated by 20-60% compared to the ASCE due to differences in Manning coefficient in urban environments.

Acknowledgements

We would like to thank Jason "Jay" Patton of the California Geological Survey and Jonathan Allan and Lalo Guerrero of the Oregon Department of Geological and Mineral Industries for providing access to the tsunami evacuation lines used by California and Oregon. We also wish to thank Randall "Randy" J LeVeque for providing us with the python notebook to create the initial tsunami conditions from the "t-shirt" models for use in GeoClaw, as well as his PTHA tutorial. We wish to thank two anonymous civil engineers for sharing and discussing the methodology of ASCE 7-22 with the authors of the study. We also wish to thank one anonymous reviewer and Steven J. Gibbons for their wonderful peer review of this manuscript. We also wish to thank Man-Yau "Joseph" Chan for the discussion on data assimilation. This work was partially funded by the Cascadia Region Earthquake Science Center (CRESCENT) through NSF-EAR award 2225286 as NASA award 9876543.

Data and code availability

Oregon tsunami related data are available at the DOGAMI Tsunami Clearing House (https://www.oregon.gov/dogami/tsuclearinghouse/Pages/default.aspx, State of Oregon, 2024). California tsunami data for Del Norte county are available at https://data.conservation.ca.gov/apps/cadoc::cgs-information-warehouse-tsunami-hazard-evacuation-map/explore and https://rctwg.humboldt.edu/. Washington state tsunami related data are available at https://www.dnr.wa.gov/programs-and-services/geology/geologic-hazards/Tsunamis. ASCE 7 tsunami data are available via the Tsunami Hazard Tool at https://asce7tsunami.online/. GeoClaw data are available at https://www.clawpack.org/geoclaw. Shuttle Radar Topography Mission (SRTM) 15+ bathymetry data were available at https://portal.opentopography.org/raster?opentopoID=

OTSRTM.122019.4326.1. CUDEM and DEM data are available at https://www.ncei.noaa.gov/maps/bathymetry/.

Competing interests

The authors have no competing interests.

References

American Society of Civil Engineers. *Minimum design loads and associated criteria for buildings and other structures*. American Society of Civil Engineers, 2022. doi: 10.1061/9780784414248.

Atwater, B. F. and Griggs, G. B. *Open File Report 2012-1043: Deep-Sea Turbidites as Guides to Holocene Earthquake history at the Cascadia Subduction Zone: Alternative Views for a Seismic-Hazard Workshop*. U.S. Department of the Interior, U.S. Geological Survey, 2012. pubs.usgs.gov/of/2012/1043/of2012-1043.pdf.

Barnhart, W. D., Murray, J. R., Briggs, R. W., Gomez, F., Miles, C. P., Svarc, J., Riquelme, S., and Stressler, B. J. Coseismic slip and early afterslip of the 2015 Illapel, Chile, earthquake: Implications for frictional heterogeneity and coastal uplift. *Journal of Geophysical Research: Solid Earth*, 121(8):6172–6191, 2016. doi: 10.1002/2016JB013124.

Becerra, I., Aránguiz, R., González, J., and Benavente, R. An improvement of tsunami hazard analysis in Central Chile based on stochastic rupture scenarios. *Coastal Engineering Journal*, 62 (4):473–488, 2020. doi: 10.1080/21664250.2020.1812943.

Boyer, M. Estimating the Manning coefficient from an average bed roughness in open channels. *Eos, Transactions American Geophysical Union*, 35(6):957–961, 1954. doi: 10.1029/TR035i006p00957.

Carbotte, S. M., Boston, B., Han, S., Shuck, B., Beeson, J., Canales, J. P., Tobin, H., Miller, N., Nedimovic, M., Tréhu, A., Lee, M., Lucas, M., Jian, H., Jiang, D., Moser, L., Anderson, C., Judd, D., Fernandez, J., Campbell, C., Goswami, A., and Gahlawat, R. Subducting plate structure and megathrust morphology from deep seismic imaging linked to earthquake rupture segmentation at Cascadia. *Science Advances*, 10(23):eadl3198, 2024. doi: 10.1126/sciadv.adl3198.

Clawpack Development Team. Clawpack Version 5.7.1, Sept. 2020. doi: 10.5281/zenodo.4025432.

Cooperative Institute for Research in Environmental Sciences. Continuously Updated Digital Elevation Model (CUDEM) - 1/9 Arc-Second Resolution Bathymetric-Topographic Tiles. doi: 10.25921/DS9V-KY35.

Davies, G. Tsunami variability from uncalibrated stochastic earthquake models: tests against deep ocean observations 2006–2016. *Geophysical Journal International*, 218(3): 1939–1960, 2019. doi: 10.1093/gji/ggz260.

Davies, G. and Griffin, J. Sensitivity of probabilistic tsunami hazard assessment to far-field earthquake slip complexity and rigidity depth-dependence: case study of Australia. *Pure and Applied Geophysics*, 177:1521–1548, 2020. doi: 10.1007/s00024-019-02299-w.

Eungard, D., Forson, C., Walsh, T., Gica, E., and Arcas, D. Tsunami hazard maps of southwest Washington—Model results from a~ 2,500-year Cascadia subduction zone earthquake scenario: Washington Geological Survey Map Series 2018-01, originally published March 2018, 6 sheets, scale 1: 48,000, 11 p. text, 2018.

Frankel, A., Chen, R., Petersen, M., Moschetti, M., and Sherrod, B. 2014 update of the Pacific Northwest portion of the US National Seismic Hazard Maps. *Earthquake Spectra*, 31(1_suppl): S131–S148, 2015. doi: 10.1193/111314EQS193M.

Geist, E. L. and Parsons, T. Probabilistic analysis of tsunami hazards. *Natural Hazards*, 37:277–314, 2006. doi: 10.1007/s11069-005-4646-z.

Goda, K. Stochastic source modeling and tsunami simulations of Cascadia subduction earthquakes for Canadian Pacific coast. *Coastal Engineering Journal*, 64(4):575–596, 2022. doi: 10.1080/21664250.2022.2139918.

Goldberg, D. E. and Melgar, D. Generation and validation of broadband synthetic P waves in semistochastic models of large earthquakes. *Bulletin of the Seismological Society of America*, 110(4): 1982–1995, 2020. doi: 10.1785/0120200049.

Goldfinger, C., Nelson, C. H., Morey, A. E., Johnson, J. E., Patton, J. R., Karabanov, E. B., Gutierrez-Pastor, J., Eriksson, A. T., Gracia, E., Dunhill, G., et al. Turbidite event history—Methods and implications for Holocene paleoseismicity of the Cascadia subduction zone. Technical report, US Geological Survey, 2012.

Goldfinger, C., Galer, S., Beeson, J., Hamilton, T., Black, B., Romsos, C., Patton, J., Nelson, C. H., Hausmann, R., and Morey, A. The importance of site selection, sediment supply, and hydrodynamics: A case study of submarine paleoseismology on the northern Cascadia margin, Washington USA. *Marine Geology*, 384:4–46, 2017. doi: 10.1016/j.margeo.2016.06.008.

Hayes, G. P. The finite, kinematic rupture properties of great-sized earthquakes since 1990. *Earth and Planetary Science Letters*, 468:94–100, 2017. doi: 10.1016/j.epsl.2017.04.003.

Hayes, G. P., Moore, G. L., Portner, D. E., Hearne, M., Flamme, H., Furtney, M., and Smoczyk, G. M. Slab2, a comprehensive subduction zone geometry model. *Science*, 362(6410):58–61, Oct. 2018. doi: 10.1126/science.aat4723.

Jaccard, P. The distribution of the flora in the alpine zone. 1. *New phytologist*, 11(2):37–50, 1912. doi: 10.1111/j.1469-8137.1912.tb05611.x.

Kelsey, H. M., Nelson, A. R., Hemphill-Haley, E., and Witter, R. C. Tsunami history of an Oregon coastal lake reveals a 4600 yr record of great earthquakes on the Cascadia subduction zone. *Geological Society of America Bulletin*, 117(7-8): 1009–1032, 2005. doi: 10.1130/B25452.1.

Koshimura, S., Oie, T., Yanagisawa, H., and Imamura, F. Developing fragility functions for tsunami damage estimation using numerical model and post-tsunami data from Banda Aceh, Indonesia. *Coastal Engineering Journal*, 51(3):243–273, 2009. doi: 10.1142/S0578563409002004.

La Selle, S. M., Nelson, A. R., Witter, R. C., Jaffe, B. E., Gelfenbaum, G., and Padgett, J. S. Testing megathrust rupture models using tsunami deposits. *Journal of Geophysical Research: Earth Surface*, 129(5):e2023JF007444, 2024. doi: 10.1029/2023JF00744https://doi.org/10.1029/2023JF0074444.

Ledeczi, A., Lucas, M., Tobin, H., Watt, J., and Miller, N. Late Quaternary Surface Displacements on Accretionary Wedge Splay Faults in the Cascadia Subduction Zone: Implications for Megathrust Rupture. *Seismica*, 2(4), Apr. 2024. doi: 10.26443/seismica.v2i4.1158.

LeVeque, R. J., Waagan, K., González, F. I., Rim, D., and Lin, G. Generating random earthquake events for probabilistic tsunami hazard assessment. *Global Tsunami Science: Past and Future, Volume I*, pages 3671–3692, 2017. doi: 10.1007/978-3-319-55480-8_2.

Li, L., Switzer, A. D., Chan, C.-H., Wang, Y., Weiss, R., and Qiu, Q. How heterogeneous coseismic slip affects regional probabilistic tsunami hazard assessment: A case study in the South China Sea. *Journal of Geophysical Research: Solid Earth*, 121(8): 6250–6272, 2016. doi: 10.1002/2016JB013111.

Li, S. and Freymueller, J. T. Spatial Variation of Slip Behavior Beneath the Alaska Peninsula Along Alaska-Aleutian Subduction Zone. *Geophysical Research Letters*, 45(8):3453–3460, Apr. 2018. doi: 10.1002/2017GL076761.

Li, S., Wang, K., Wang, Y., Jiang, Y., and Dosso, S. E. Geodetically inferred locking state of the Cascadia megathrust based on a viscoelastic Earth model. *Journal of Geophysical Research: Solid Earth*, 123(9):8056–8072, 2018. doi: 10.1029/2018JB015620.

Lindsey, E. O., Mallick, R., Hubbard, J. A., Bradley, K. E., Almeida, R. V., Moore, J. D., Bürgmann, R., and Hill, E. M. Slip rate deficit and earthquake potential on shallow megathrusts. *Nature Geoscience*, 14(5):321–326, 2021. doi: 10.1038/s41561-021-00736-x.

Loveless, J. P. and Meade, B. J. Kinematic barrier constraints on the magnitudes of additional great earthquakes off the east coast of Japan. *Seismological Research Letters*, 86(1):202–209, 2015. doi: 10.1785/0220140083.

Ma, S. and Nie, S. Dynamic Wedge Failure and Along-Arc Variations of Tsunamigenesis in the Japan Trench Margin. *Geophysical Research Letters*, 46(15):8782–8790, Aug. 2019. doi: 10.1029/2019GL083148.

Mai, P. M. and Thingbaijam, K. K. S. SRCMOD: An Online Database of Finite-Fault Rupture Models. *Seismological Research Letters*, 85(6):1348–1357, Oct. 2014. doi: 10.1785/0220140077.

Melgar, D. Was the January 26th, 1700 Cascadia earthquake part of a rupture sequence? *Journal of Geophysical Research: Solid Earth*, 126(10):e2021JB021822, 2021. doi: 10.1029/2021JB021822.

Melgar, D., Fan, W., Riquelme, S., Geng, J., Liang, C., Fuentes, M., Vargas, G., Allen, R. M., Shearer, P. M., and Fielding, E. J. Slip segmentation and slow rupture to the trench during the 2015, M_w 8.3 Illapel, Chile earthquake. *Geophysical Research Letters*, 43(3):961–966, Feb. 2016a. doi: 10.1002/2015GL067369.

Melgar, D., LeVeque, R. J., Dreger, D. S., and Allen, R. M. Kinematic rupture scenarios and synthetic displacement data: An example application to the Cascadia subduction zone. *Journal of Geophysical Research: Solid Earth*, 121(9):6658–6674, 2016b. doi: 10.1002/2016JB013314.

Melgar, D., Williamson, A. L., and Salazar-Monroy, E. F. Differences between heterogenous and homogenous slip in regional tsunami hazards modelling. *Geophysical Journal International*, 219(1):553–562, 2019. doi: 10.1093/gji/ggz299.

Métois, M., Socquet, A., Vigny, C., Carrizo, D., Peyrat, S., Delorme, A., Maureira, E., Valderas-Bermejo, M.-C., and Ortega, I. Revisiting the North Chile seismic gap segmentation using GPS-derived interseismic coupling. *Geophysical Journal International*, 194(3):1283–1294, 2013. doi: 10.1093/gji/ggt183.

Mori, N., Takahashi, T., Yasuda, T., and Yanagisawa, H. Survey of 2011 Tohoku earthquake tsunami inundation and run-up. *Geophysical research letters*, 38(7), 2011. doi: 10.1029/2011GL049210.

Mori, N., Satake, K., Cox, D., Goda, K., Catalan, P. A., Ho, T.-C., Imamura, F., Tomiczek, T., Lynett, P., Miyashita, T., et al. Giant tsunami monitoring, early warning and hazard assessment. *Nature Reviews Earth & Environment*, 3(9):557–572, 2022. doi: 10.1038/s43017-022-00327-3.

Nelson, A. R., DuRoss, C. B., Witter, R. C., Kelsey, H. M., Engelhart, S. E., Mahan, S. A., Gray, H. J., Hawkes, A. D., Horton, B. P., and Padgett, J. S. A maximum rupture model for the central and southern Cascadia subduction zone—reassessing ages for coastal evidence of megathrust earthquakes and tsunamis. *Quaternary Science Reviews*, 261:106922, 2021. doi: 10.1016/j.quascirev.2021.106922.

NOAA National Geophysical Data Center. 2010: Crescent City, California 1/3 arc-second MHW Coastal Digital Elevation Model. https://www.ncei.noaa.gov/access/metadata/landing-page/bin/iso?id=gov.noaa.ngdc.mgg.dem:693.

Perfettini, H., Avouac, J.-P., Tavera, H., Kositsky, A., Nocquet, J.-M., Bondoux, F., Chlieh, M., Sladen, A., Audin, L., Farber, D. L., et al. Seismic and aseismic slip on the Central Peru megathrust. *Nature*, 465(7294):78–81, 2010. doi: 10.1038/nature09062.

Petersen, M. D., Shumway, A. M., Powers, P. M., Field, E. H., Moschetti, M. P., Jaiswal, K. S., Milner, K. R., Rezaeian, S., Frankel, A. D., Llenos, A. L., et al. The 2023 US 50-state national seismic hazard model: Overview and implications. *Earthquake Spectra*, 40(1):5–88, 2024. doi: 10.1177/87552930231215428.

Priest, G. R. *Explanation of mapping methods and use of the tsunami hazard maps of the Oregon coast*. Number 0-67. State of Oregon, Department of Geology and Mineral Industries, 1995. https://d3itl75cn7661p.cloudfront.net/dogami/ofr/O-95-67.pdf.

Priest, G. R. and Allan, J. C. *Comparison of Oregon tsunami hazard scenarios to a probabilistic tsunami hazard analysis (PTHA)*. Oregon Department of Geology and Mineral Industries, 2019. https://d3itl75cn7661p.cloudfront.net/dogami/ofr/O-19-04_report.pdf.

Schmalzle, G. M., McCaffrey, R., and Creager, K. C. Central Cascadia subduction zone creep. *Geochemistry, Geophysics, Geosystems*, 15(4):1515–1532, 2014. doi: 10.1002/2013GC005172.

Sepúlveda, I., Liu, P. L.-F., Grigoriu, M., and Pritchard, M. Tsunami hazard assessments with consideration of uncertain earthquake slip distribution and location. *Journal of Geophysical Research: Solid Earth*, 122(9):7252–7271, 2017. doi: 10.1002/2017JB014430.

Small, D. T. and Melgar, D. Geodetic coupling models as constraints on stochastic earthquake ruptures: An example application to PTHA in Cascadia. *Journal of Geophysical Research: Solid Earth*, 126(7):e2020JB021149, 2021. doi: 10.1029/2020JB021149.

Small, D. T. and Melgar, D. Can stochastic slip rupture modeling produce realistic M9+ events? *Journal of Geophysical Research: Solid Earth*, 128(3):e2022JB025716, 2023. doi: 10.1029/2022JB025716.

State of California. *Tsunami Hazard Area, Del Norte County; produced by the California Geological Survey and the California Governor's Office of Emergency Services*. California Department of Conservation, California, 2022.

State of Oregon. Oregon Department of Geology and Mineral Industries : Oregon Tsunami Clearinghouse : Oregon Tsunami Clearinghouse : State of Oregon — oregon.gov. https://www.oregon.gov/dogami/tsuclearinghouse/pages/tsunami-evacuation-maps.aspx, 2024. [Accessed 06-11-2024].

Sypus, M. and Wang, K. IMPROVED CASCADIA EARTHQUAKE SOURCE MODELS FOR TSUNAMI HAZARD ASSESSMENT. *Oregon department of geology and mineral industries open-file report O-24-11*, 2024. https://www.oregon.gov/dogami/pubs/pages/ofr/p-o-24-11.aspx.

Takagi, H. and Bricker, J. D. Assessment of the effectiveness of general breakwaters in reducing tsunami inundation in Ishinomaki. *Coastal Engineering Journal*, 56(4):1450018–1, 2014. doi: 10.1142/S0578563414500181.

Tanioka, Y., Ruff, L., and Satake, K. What controls the lateral variation of large earthquake occurrence along the Japan Trench? *The Island Arc*, 6(3):261–266, Sept. 1997. doi: 10.1111/j.1440-1738.1997.tb00176.x.

Thio, H. K. and Somerville, P. *A Probabilistic Tsunami Hazard Analysis of California*, pages 1–12. ASCE, 2009. doi: 10.1061/41050(357)57.

Tozer, B., Sandwell, D. T., Smith, W. H. F., Olson, C., Beale, J. R., and

Wessel, P. Global Bathymetry and Topography at 15 Arc Sec: SRTM15+. *Earth and Space Science*, 6(10):1847–1864, Oct. 2019. doi: 10.1029/2019EA000658.

Van Leeuwen, P. J. Particle filtering in geophysical systems. *Monthly Weather Review*, 137(12):4089–4114, 2009. doi: 10.1175/2009MWR2835.1.

Villegas-Lanza, J. C., Chlieh, M., Cavalié, O., Tavera, H., Baby, P., Chire-Chira, J., and Nocquet, J.-M. Active tectonics of Peru: Heterogeneous interseismic coupling along the Nazca megathrust, rigid motion of the Peruvian Sliver, and Subandean shortening accommodation. *Journal of Geophysical Research: Solid Earth*, 121(10):7371–7394, 2016. doi: 10.1002/2016JB013080.

Walton, M. A., Staisch, L. M., Dura, T., Pearl, J. K., Sherrod, B., Gomberg, J., Engelhart, S., Tréhu, A., Watt, J., Perkins, J., et al. Toward an integrative geological and geophysical view of Cascadia subduction zone earthquakes. *Annual Review of Earth and Planetary Sciences*, 49(1):367–398, 2021. doi: 10.1146/annurev-earth-071620-065605.

Wessel, P., Luis, J. F., Uieda, L. a., Scharroo, R., Wobbe, F., Smith, W. H., and Tian, D. The generic mapping tools version 6. *Geochemistry, Geophysics, Geosystems*, 20(11):5556–5564, 2019. doi: 10.1029/2019GC008515.

Williamson, A., Melgar, D., and Rim, D. The Effect of Earthquake Kinematics on Tsunami Propagation. *Journal of Geophysical Research: Solid Earth*, 124(11):11639–11650, Nov. 2019. doi: 10.1029/2019JB017522.

Witter, R. C., Zhang, Y., Wang, K., Priest, G. R., Goldfinger, C., Stimely, L. L., English, J. T., and Ferro, P. A. Simulating tsunami inundation at Bandon, Coos County, Oregon, using hypothetical Cascadia and Alaska earthquake scenarios. *Oregon department of geology and mineral industries special paper*, 43:57, 2011.

Witter, R. C., Zhang, Y. J., Wang, K., Priest, G. R., Goldfinger, C., Stimely, L., English, J. T., and Ferro, P. A. Simulated tsunami inundation for a range of Cascadia megathrust earthquake scenarios at Bandon, Oregon, USA. *Geosphere*, 9(6):1783–1803, Dec. 2013. doi: 10.1130/GES00899.1.

Ye, L., Lay, T., Kanamori, H., and Rivera, L. Rupture characteristics of major and great ($M \geq 7.0$) megathrust earthquakes from 1990 to 2015: 1. Source parameter scaling relationships. *Journal of Geophysical Research: Solid Earth*, 121(2):826–844, 2016. doi: 10.1002/2015JB012426.

Yun, N. Y. and Hamada, M. Evacuation behavior and fatality rate during the 2011 Tohoku-Oki earthquake and tsunami. *Earthquake Spectra*, 31(3):1237–1265, 2015.

The article *Comparisons of tsunami inundation for homogeneous and heterogeneous earthquake sources at selected sites for the Cascadia Subduction Zone* © 2026 by Sean R. Santellanes is licensed under CC BY 4.0.